

**ALMA Lensing Cluster Survey:  
Bright [C II] 158  $\mu$ m Lines from a Multiply Imaged Sub- $L^*$  Galaxy at  $z = 6.0719$**

SEIJI FUJIMOTO,<sup>1,2</sup> MASAMUNE OGURI,<sup>3,4,5</sup> GABRIEL BRAMMER,<sup>1,2</sup> YUKI YOSHIMURA,<sup>6,7</sup> NICOLAS LAPORTE,<sup>8,9</sup>  
JORGE GONZÁLEZ-LÓPEZ,<sup>10,11</sup> GABRIEL B. CAMINHA,<sup>12</sup> KOTARO KOHNO,<sup>7,13</sup> ADI ZITRIN,<sup>14</sup> JOHAN RICHARD,<sup>15</sup>  
MASAMI OUCHI,<sup>16,17,5</sup> FRANZ E. BAUER,<sup>18,19</sup> IAN SMAIL,<sup>20</sup> BUNYO HATSUKADE,<sup>7</sup> YOSHIKI ONO,<sup>17</sup> VASILY KOKOREV,<sup>1,2</sup>  
HIDEKI UMEHATA,<sup>21,7</sup> DANIEL SCHAERER,<sup>22,23</sup> KIRSTEN KNUDSEN,<sup>24</sup> FENGWU SUN,<sup>25</sup> GEORGIOS MAGDIS,<sup>1,2,26</sup>  
FRANCESCO VALENTINO,<sup>1,2</sup> YIPING AO,<sup>27</sup> SUNE TOFT,<sup>1,2</sup> MIROSLAVA DESSAUGES-ZAVADSKY,<sup>22</sup> KAZUHIRO SHIMASAKU,<sup>6,3</sup>  
KARINA CAPUTI,<sup>28,1</sup> HARUKA KUSAKABE,<sup>22</sup> KANA MOROKUMA-MATSUI,<sup>7</sup> KIKUCHIHARA SHOTARO,<sup>6,17</sup> EIICHI EGAMI,<sup>25</sup>  
MINJU M. LEE,<sup>29</sup> TIMOTHY RAWLE,<sup>30</sup> AND DANIEL ESPADA<sup>31</sup>

<sup>1</sup> *Cosmic Dawn Center (DAWN), Jagtvej 128, DK2200 Copenhagen N, Denmark*

<sup>2</sup> *Niels Bohr Institute, University of Copenhagen, Lyngbyvej 2, DK2100 Copenhagen Ø, Denmark*

<sup>3</sup> *Research Center for the Early Universe, Graduate School of Science, The University of Tokyo, 7-3-1 Hongo, Bunkyo-ku, Tokyo 113-0033, Japan*

<sup>4</sup> *Department of Physics, The University of Tokyo, 7-3-1 Hongo, Bunkyo-ku, Tokyo 113-0033, Japan*

<sup>5</sup> *Kavli Institute for the Physics and Mathematics of the Universe (WPI), The University of Tokyo, 5-1-5 Kashiwanoha, Kashiwa-shi, Chiba, 277-8583, Japan*

<sup>6</sup> *Department of Astronomy, Graduate School of Science, The University of Tokyo, 7-3-1 Hongo, Bunkyo-ku, Tokyo 113-0033, Japan*

<sup>7</sup> *Institute of Astronomy, Graduate School of Science, The University of Tokyo, 2-21-1 Osawa, Mitaka, Tokyo 181-0015, Japan*

<sup>8</sup> *Kavli Institute for Cosmology, University of Cambridge, Madingley Road, Cambridge CB3 0HA, UK*

<sup>9</sup> *Cavendish Laboratory, University of Cambridge, 19 JJ Thomson Avenue, Cambridge CB3 0HE, UK*

<sup>10</sup> *Núcleo de Astronomía de la Facultad de Ingeniería y Ciencias, Universidad Diego Portales, Av. Ejército Libertador 441, Santiago, Chile*

<sup>11</sup> *Las Campanas Observatory, Carnegie Institution of Washington, Casilla 601, La Serena, Chile*

<sup>12</sup> *Kapteyn Astronomical Institute, University of Groningen, Postbus 800, 9700 AV Groningen, The Netherlands*

<sup>13</sup> *Research Center for the Early Universe, School of Science, The University of Tokyo, 7-3-1 Hongo, Bunkyo-ku, Tokyo 113-0033, Japan*

<sup>14</sup> *Physics Department, Ben-Gurion University of the Negev, P.O. Box 653, Be'er-sheva 8410501, Israel*

<sup>15</sup> *Univ Lyon, Univ Lyon1, Ens de Lyon, CNRS, Centre de Recherche Astrophysique de Lyon UMR5574, F-69230, Saint-Genis-Laval, France*

<sup>16</sup> *National Astronomical Observatory of Japan, 2-21-1 Osawa, Mitaka, Tokyo 181-8588, Japan*

<sup>17</sup> *Institute for Cosmic Ray Research, The University of Tokyo, 5-1-5 Kashiwanoha, Kashiwa, Chiba 277-8582, Japan*

<sup>18</sup> *Instituto de Astrofísica, Facultad de Física, Pontificia Universidad Católica de Chile Av. Vicuña Mackenna 4860, 782-0436 Macul, Santiago, Chile*

<sup>19</sup> *Millennium Institute of Astrophysics (MAS), Nuncio Monse nor Santero Sanz 100, Providencia, Santiago, Chile*

<sup>20</sup> *Centre for Extragalactic Astronomy, Department of Physics, Durham University, South Road, Durham DH1 3LE, UK*

<sup>21</sup> *RIKEN Cluster for Pioneering Research, 2-1 Hirosawa, Wako, Saitama 351-0198, Japan*

<sup>22</sup> *Observatoire de Genève, Université de Genève, 51 Ch. des Maillettes, 1290 Versoix, Switzerland*

<sup>23</sup> *CNRS, IRAP, 14 Avenue E. Belin, 31400 Toulouse, France*

<sup>24</sup> *Department of Space, Earth and Environment, Chalmers University of Technology, Onsala Space Observatory, SE-43992 Onsala, Sweden*

<sup>25</sup> *Steward Observatory, University of Arizona, 933 N. Cherry Ave, Tucson, AZ 85721, USA*

<sup>26</sup> *DTU-Space, Technical University of Denmark, Elektrovej 327, DK2800 Kgs. Lyngby, Denmark*

<sup>27</sup> *Purple Mountain Observatory and Key Laboratory for Radio Astronomy, Chinese Academy of Sciences, Nanjing, China*

<sup>28</sup> *Kapteyn Astronomical Institute, University of Groningen, P.O. Box 800, 9700AV Groningen, The Netherlands*

<sup>29</sup> *Max-Planck-Institut für Extraterrestrische Physik (MPE), Giessenbachstr., D-85748, Garching, Germany.*

<sup>30</sup> *European Space Agency (ESA), ESA Office, Space Telescope Science Institute, 3700 San Martin Drive, Baltimore, MD 21218, USA*

<sup>31</sup> *SKA Organisation, Lower Withington, Macclesfield, Cheshire SK11 9DL, UK*

(Received 2020 October 14; Revised 2020 December 14; Accepted 2020 December 29)

ApJ in press

## ABSTRACT

We present bright [C II] 158  $\mu\text{m}$  line detections from a strongly magnified and multiply-imaged ( $\mu \sim 20\text{--}160$ ) sub- $L^*$  ( $M_{\text{UV}} = -19.75^{+0.55}_{-0.44}$ ) Lyman-break galaxy (LBG) at  $z = 6.0719 \pm 0.0004$  from the ALMA Lensing Cluster Survey (ALCS). Emission lines are identified at 268.7 GHz at  $\geq 8\sigma$  exactly at positions of two multiple images of the LBG behind the massive galaxy cluster RXCJ0600–2007. Our lens models, updated with the latest spectroscopy from VLT/MUSE, indicate that a sub region of the LBG crosses the caustic and is lensed into a long ( $\sim 6''$ ) arc with a local magnification of  $\mu \sim 160$ , for which the [C II] line is also significantly detected. The source-plane reconstruction resolves the interstellar medium (ISM) structure, showing that the [C II] line is co-spatial with the rest-frame UV continuum at the scale of  $\sim 300$  pc. The [C II] line properties suggest that the LBG is a rotation-dominated system whose velocity gradient explains a slight difference of redshifts between the whole LBG and its sub region. The star formation rate (SFR)– $L_{[\text{C II}]}$  relations from the sub to the whole regions of the LBG are consistent with those of local galaxies. We evaluate the lower limit of the faint-end of the [C II] luminosity function at  $z = 6$ , and find that it is consistent with predictions from semi analytical models and from the local SFR– $L_{[\text{C II}]}$  relation with a SFR function at  $z = 6$ . These results imply that the local SFR– $L_{[\text{C II}]}$  relation is universal for a wide range of scales including the spatially resolved ISM, the whole region of galaxy, and the cosmic scale, even in the epoch of reionization.

*Keywords:* galaxies: formation — galaxies: evolution — galaxies: high-redshift — galaxies: ISM — galaxies: kinematics and dynamics — galaxies: luminosity function

## 1. INTRODUCTION

Galaxy evolution is regulated by several key mechanisms in the interstellar medium (ISM) such as disk formation, stellar and active galactic nuclei (AGN) feedback, mass building via star formation and galaxy mergers, and clump formations through disk instabilities. Resolving the ISM structure to study local physical properties in high-redshift galaxies is thus essential in order to understand the initial phase of galaxy formation and evolution.

During the past decades, hundreds of star-forming galaxies at  $z > 6$  have been spectroscopically identified mainly with Ly $\alpha$  lines (e.g., Iye et al. 2006; Vanzella et al. 2011; Pentericci et al. 2011, 2014, 2018; Shibuya et al. 2012, 2018; Ono et al. 2012, 2018; Finkelstein et al. 2013; Oesch et al. 2015, 2016; Stark et al. 2017; Higuchi et al. 2019). The Atacama Large Millimeter/submillimeter Array (ALMA) offers a rest-frame far-infrared (FIR) spectroscopic window for these  $z > 6$  galaxies, especially with bright fine-structure lines of [C II] 158  $\mu\text{m}$  and [O III] 88  $\mu\text{m}$  (e.g., Maiolino et al. 2015; Inoue et al. 2016; Pentericci et al. 2016; Knudsen et al. 2016; Matthee et al. 2017, 2019; Carniani et al. 2018; Smit et al. 2018; Bowler et al. 2018; Hashimoto et al. 2018, 2019; Tamura et al. 2019; Fujimoto et al. 2019; Bakx et al. 2020). Since heavy elements produced in stars are returned into the ISM, the metal gas properties traced by the fine-structure lines are good probes of the star-formation history and related physical mech-

anisms (Maiolino & Mannucci 2019). In fact, recent ALMA spatial and kinematic [C II]-line studies identify signatures of some key mechanisms, including disk rotations (e.g., Jones et al. 2017; Smit et al. 2018), galaxy mergers (e.g., Hashimoto et al. 2019; Le Fèvre et al. 2020), and outflows (e.g., Gallerani et al. 2018; Spilker et al. 2018; Fujimoto et al. 2019, 2020b; Ginolfi et al. 2020). In conjunction with other fine-structure lines of [O III] and [N II], recent ALMA observations also allow us to perform multiple line diagnostics to constrain the dominant ionization state of the ISM gas (e.g., Inoue et al. 2016; Pavesi et al. 2016; Laporte et al. 2019; Novak et al. 2019; Harikane et al. 2020).

There are several challenges related to the FIR spectroscopy. The first is sensitivity. While ALMA is the most sensitive mm/submm telescope and yielding a large number of new findings about high-redshift galaxies, the detection of FIR fine-structure lines from abundant, typical galaxies remains challenging. For example, to observe a [C II] line of  $\sim 1 \times 10^8 L_{\odot}$  from  $z = 6$ , about 2-hour observing time is required<sup>1</sup>. However, such a source typically falls in the absolute UV magnitude range of  $M_{\text{UV}} \sim -22.0 - -21.5$  mag (see e.g., Table 7 in Hashimoto et al. 2019). This absolute UV magnitude

<sup>1</sup> Based on CASA Observing Tool calculations to detect the [C II] line of  $1 \times 10^8 L_{\odot}$  with a line width of 200 km s<sup>-1</sup> at  $\geq 5\sigma$  in the velocity integrated map.

range is  $\sim 2\text{--}3$  times brighter than the characteristic luminosity  $L^*$  in the UV luminosity function at  $z > 6$  (e.g., Ono et al. 2018), indicating that  $\gtrsim 10$ -hour observing time is necessary to study the abundant, typical galaxies with  $L^*$  or sub- $L^*$  luminosities. The second challenge is high spatial resolution observations towards these typical galaxies. Recent *Hubble Space Telescope* (*HST*) studies report that the typical effective radius ( $r_e$ ) in star-forming galaxies at  $z > 6$  is estimated to be  $< 1$  kpc ( $\simeq 0''.2$ ) (e.g., Holwerda et al. 2015; Shibuya et al. 2015; Bouwens et al. 2017; Kawamata et al. 2018). The ISM structure mostly comparable to the  $r_e$  scale could be resolved by ALMA high-resolution observations down to the  $0''.02$  scale. However, this requires even longer observing times than  $\gtrsim 10$  hours estimated above just for the detection of the typical galaxies. The third challenge is the requirement of prior spectroscopic redshifts due to the narrow frequency coverage of ALMA (7.5-GHz coverage in a single tuning), which may cause potential biases. In most cases, the prior spectroscopic redshift is obtained from Ly $\alpha$  lines. While high-redshift galaxies with Ly $\alpha$  spectroscopic redshifts show weak [C II] lines at a given star-formation rate (Carniani et al. 2018; Harikane et al. 2018, 2020; cf. Schaerer et al. 2020), a recent study by Smit et al. (2018) indicates that galaxies with no strong Ly $\alpha$  line may emit a strong [C II] line. Because the fraction of Ly $\alpha$  emitters (LAEs; e.g., equivalent width of Ly $\alpha > 25$  Å) is less than 30% among star-forming galaxies with  $M_{\text{UV}} \sim -21.5$  mag at  $z > 6$  (e.g., Stark et al. 2011; Treu et al. 2013; Tilvi et al. 2014; De Barros et al. 2017; Pentericci et al. 2018; Kusakabe et al. 2020), follow-up observations of galaxies only with secure Ly $\alpha$  lines will systematically miss a majority of the representative population at  $z > 6$ . An ALMA blind line survey is one possible solution, but novel [C II] line emitters  $z > 6$  have not yet been identified due to the lack of sufficiently deep and large survey volumes (e.g., Matsuda et al. 2015; Aravena et al. 2016; Yamaguchi et al. 2017; Hayatsu et al. 2019; Yan et al. 2020; Romano et al. 2020; Decarli et al. 2020).

In this paper, we report the blind detection of bright [C II] 158- $\mu\text{m}$  lines from strongly lensed multiple images of a sub- $L^*$  galaxy at  $z = 6.0719$  behind the massive galaxy cluster RXCJ0600–2007, drawn from ALMA Lensing Cluster Survey (ALCS). Making full use of large ancillary data sets, including *HST*, *Spitzer*, and VLT and with help of gravitational lensing magnification, we resolve the ISM structures and investigate the spatially resolved rest-frame UV-to-FIR continuum and the [C II] line properties down to a  $\simeq 300$  pc scale. This is the first ALMA study to resolve the ISM properties in a representative ( $\simeq$  sub- $L^*$ ) galaxy in the epoch of reionization.

The structure of this paper is as follows. In Section 2, we overview the ALCS survey and the data sets in RXCJ0600–2007 as well as strong lensing mass models of the cluster. Section 3 outlines methods of the blind line identification and optical–near infrared (NIR) properties of the two [C II] line emitters at  $z = 6.07$ . In Section 4, we report and discuss intrinsic characteristics of these two [C II] line emitters with the correction of the lensing magnification. A summary of this study is presented in Section 5. Throughout this paper, we assume the Chabrier initial mass function (Chabrier 2003) and a flat universe with  $\Omega_m = 0.3$ ,  $\Omega_\Lambda = 0.7$ ,  $\sigma_8 = 0.8$ , and  $H_0 = 70$  km s $^{-1}$  Mpc $^{-1}$ . We use magnitudes in the AB system (Oke & Gunn 1983).

## 2. DATA AND REDUCTION

### 2.1. ALMA Lensing Cluster Survey

ALCS is a cycle-6 ALMA large program (Project ID: 2018.1.00035.L; PI: K. Kohno) to map a total of 88-arcmin $^2$  high-magnification regions in 33 massive galaxy clusters at 1.2-mm in Band 6. The sample is selected from the best-studied clusters drawn from *HST* treasury programs, i.e., the Cluster Lensing And Supernova Survey with Hubble (CLASH; Postman et al. 2012), Hubble Frontier Fields (HFF; Lotz et al. 2017), and the Reionization Lensing Cluster Survey (RELICS; Coe et al. 2019). Observations were carried out between December 2018 and December 2019 in compact array configurations of C43-1 and C43-2 fine tuned to recover strongly lensed (i.e., spatially elongated), low surface brightness sources. The 1.2-mm mapping is accomplished with a 15-GHz wide spectral scan in the ranges of 250.0–257.5 GHz and 265.0–272.5 GHz via two frequency setups to enlarge the survey volume for line-emitting galaxies. The spectral mode of Time Division Mode is used, which achieves the spectral resolution of  $\sim 28$  km s $^{-1}$  through these frequency setups. A full description of the survey and of its main objectives will be presented in a separate paper (in preparation).

### 2.2. RXCJ0600–2007

RXCJ0600–2007 is a massive ( $\sim 10^{15} M_\odot$ ) galaxy cluster at  $z = 0.43$  that is included in RELICS and was firstly identified in the Massive Cluster Survey (MACS; Ebeling et al. 2001). As a part of ALCS, the ALMA observations for RXCJ0600–2007 were performed in January 2019, mapping the central area of  $230'' \times 90''$  in 105 pointings with 46–49 12-m antennae providing baselines of 15–456 m under a precipitable water vapor (PWV) of 0.6–1.3 mm. J0522-3627 was observed as a flux calibrator. The bandpass and phase calibrations were performed with J0609-1542.

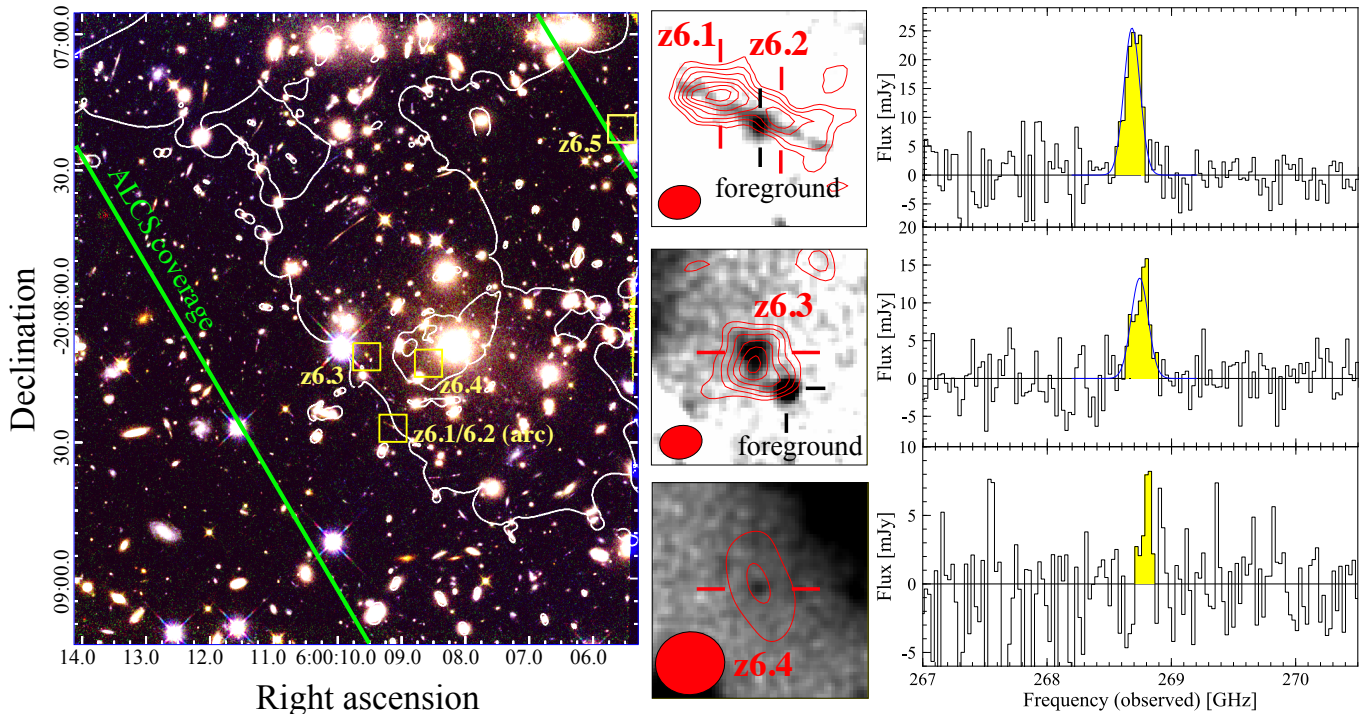


**Figure 1.** **Left:** False-color *HST* image of the cluster RXCJ0600–2007 (red: F160W, green: F125W, blue: F814W). The white line denotes the critical curve at  $z = 6.07$  estimated from our fiducial mass model. The green lines indicate the ALCS area coverage in this cluster, within which the relative sensitivity to the deepest part of the cluster is greater than 30%. The five multiple image positions of RXCJ0600- $z_6$  are marked with the yellow  $6'' \times 6''$  squares. **Middle:** *HST*/F160W  $6'' \times 6''$  cutouts for the multiple images of  $z_6.1/6.2$ ,  $z_6.3$ , and  $z_6.4$  from top to bottom. The red contours denote the velocity-integrated [C II] line intensity drawn at  $1\sigma$  intervals from  $\pm 2\sigma$  to  $\pm 8\sigma$ . We use the natural-weighted map for  $z_6.1/6.2$  and  $z_6.3$ , while we use the  $uv$ -tapered ( $1''.8 \times 1''.8$ ) map for  $z_6.4$  to obtain the optimized S/N. The ALMA synthesized beams are presented in the bottom left. The black bars indicate foreground sources. The foreground source overlapping  $z_6.1/6.2$  is subtracted in our optical-NIR analysis with GALFIT (see Section 3.2 and Appendix C. see also N. Laporte et al. submitted). **Right:** [C II] line spectra for  $z_6.1/6.2$ ,  $z_6.3$ , and  $z_6.4$  from top to bottom that we obtain in the ALCS data cube. The yellow shade indicates the [C II] integration range for the velocity-integrated map whose contours are shown in the middle panel. The blue curve is the best-fit single Gaussian.

The ALMA data were reduced and calibrated with the Common Astronomy Software Applications package version 5.4.0 (CASA; McMullin et al. 2007) with the pipeline script in the standard manner. With the CASA task TCLEAN, continuum maps were produced by utilizing all spectral windows. The TCLEAN routines were executed down to the  $3\sigma$  level. We adopted a pixel scale of  $0''.15$  and a common spectral channel bin of  $30 \text{ km s}^{-1}$ . The natural-weighted map achieved a synthesized beam FWHM of  $1''.22 \times 0''.95$  with sensitivities in the continuum and the line in a  $30\text{-km s}^{-1}$  width channel of  $56.9$  and  $932 \mu\text{Jy beam}^{-1}$ , respectively. We also produced several  $uv$ -tapered maps in a parameter range of  $0''.8 \times 0''.8$  to  $1''.8 \times 1''.8$  to obtain spatially integrated properties when necessary. Throughout the paper, we used the natural-weighted map unless mentioned otherwise.

*HST*/ACS–WFC3 and *Spitzer*/IRAC observations were carried out as a part of RELICS (Coe et al. 2019) and *Spitzer*-RELICS (Strait et al. 2020) surveys, respec-

tively. *HST* images were obtained in the F606W (2180 s), F814W (3565 s), F105W (1411 s), F125W (711 s), F140W (736 s), and F160W (1961 s) filters. The IRAC channel 1 ( $3.6 \mu\text{m}$ ) and channel 2 ( $4.5 \mu\text{m}$ ) integrations are approximately 10 hours each. We aligned all of the *HST* exposures to sources in the PanSTARRS (DR1) catalog (Chambers et al. 2016; Flewelling et al. 2016)—which we verified is consistent with the *Gaia* DR2 (Gaia Collaboration et al. 2018) astrometric frame—and created final mosaics in a common pixel frame with  $50 \text{ mas}$  and  $100 \text{ mas}$  pixels for the ACS/WFC and WFC3/IR filters respectively. We aligned the individual *Spitzer* exposures to the same astrometric frame and generated final drizzled IRAC mosaics with a pixel scale of  $0''.5$ . Further details of the *HST* (*Spitzer*) image processing with the *grizli* (*golfir*) software will be presented in Kokorev et al. (in prep). In Figure 1, we present the false-color *HST* image of RXCJ0600–2007.

**Table 1.** Observed FIR properties of bright [C II] line emitters identified in RXCJ0600–2007

Name	$z6.1/6.2$ (arc) <sup>†</sup>	$z6.3$	$z6.4$	$z6.5$ <sup>‡</sup>
R.A.	06:00:09.13	06:00:09.55	06:00:08.58	06:00:05.55
Dec.	−20:08:26.49	−20:08:11.26	−20:08:12.54	−20:07:20.86
S/N	9.2	8.0	3.0	–
$\nu_{\text{center}}$ [GHz]	$268.682 \pm 0.011$	$268.744 \pm 0.016$	$(268.744)^{\dagger\dagger}$	–
FWHM [km s <sup>−1</sup> ]	$169 \pm 22$	$181 \pm 34$	$(181)^{\dagger\dagger}$	–
$z_{\text{[CII]}}$	$6.0736 \pm 0.0003$	$6.0719 \pm 0.0004$	$(6.0719)^{\dagger\dagger}$	–
$S_{\text{[CII]}}$ [Jy km s <sup>−1</sup> ]	$4.83 \pm 0.62$	$2.75 \pm 0.20$	$0.44 \pm 0.20$	–
$L_{\text{[CII]}}$ [ $\times 10^9 L_{\odot}$ ]	$4.5 \pm 0.40$	$2.3 \pm 0.21$	$0.42 \pm 0.19$	–
$f_{1.2\text{mm}}$ [mJy]	$0.35 \pm 0.08$	$0.20 \pm 0.08$	< 0.16	–
[C II] major-axis [″]	$4.24 \pm 0.82$	$1.17 \pm 0.29$	– <sup>††</sup>	–
[C II] minor-axis [″]	$0.63 \pm 0.51$	$0.88 \pm 0.43$	– <sup>††</sup>	–
[C II] position angle [°]	$71 \pm 5$	$8 \pm 430$	– <sup>††</sup>	–

NOTE— **S/N**: Signal-to-noise ratio at the peak pixel in the natural-weighted map, after velocity integration. The velocity integration range is denoted by the yellow shaded region in the right panel of Figure 1.  **$\nu_{\text{center}}$  & FWHM**: [C II] line peak frequency and full-width-at-half-maximum estimated from a single Gaussian fit.  **$z_{\text{[CII]}}$** : Redshift of the [C II] line emission estimated from the frequency peak.  **$S_{\text{[CII]}}$  &  $L_{\text{[CII]}}$** : The velocity integrated [C II] line intensity and the line luminosity with optimized apertures. Here we adopt a velocity integration range of  $1.5 \times \text{FWHM}$ .  **$f_{1.2\text{mm}}$** : Peak 1.2-mm continuum flux density in a  $uv$ -tapered ( $2''.0 \times 2''.0$ ) map. We provide a  $2\sigma$  upper limit for  $z6.4$ . **[C II] major-/minor-axis & position angle**: Deconvolved spatial size (in FWHM) and position angle of the [C II] line in the velocity-integrated map measured with IMFIT. For  $z6.1/6.2$ , we use a  $uv$ -tapered ( $1''.0 \times 1''.0$ ) map to obtain the global scale property.

<sup>†</sup> This source is called also as RXCJ0060-arc in N. Laporte et al. (submitted).

<sup>††</sup> We do not perform any profile fitting to the spectrum and the 2D spatial map of  $z6.4$  due to its faintness. We adopt the FWHM and the peak frequency based on  $z6.3$  for calculating the velocity-integrated intensity of the line.

<sup>‡</sup>  $z6.5$  falls outside of the ALCS area coverage.

VLT/MUSE integral field spectroscopy of the RXCJ0600–2007 field was obtained on 26th January 2018 (ESO program ID 0100.A-0792, P.I.: A. Edge). The 0.8-hour observation was split in three exposures of 970 seconds each, centered on the brightest cluster galaxy (BCG) covering 1 arcmin<sup>2</sup> of the cluster core. We use the standard MUSE reduction pipeline version 2.8.1 (Weilbacher et al. 2014) to create the final data-cube. In this process, we used the self-calibration method based on the MUSE Python Data Analysis Framework (Bacon et al. 2016; Piqueras et al. 2017) and implemented in this version of the reduction pipeline. Finally, we applied the Zurich Atmosphere Purge (ZAP, Soto et al. 2016) to remove the sky residuals that were not completely removed by the MUSE pipeline.

We used the MUSE data cube to build our redshift catalog in two steps, similar to Caminha et al. (2017, 2019). We first extracted the spectra of all sources detected in the *HST* imaging, and in a second step, we performed a blind search for faint-line emitters. This procedure allowed us to measure 76 secure redshifts, of which 16 are emission from galaxies behind the cluster. This redshift catalogue was used to identify cluster members and multiply imaged galaxies that were used in strong lens mass modeling (see Section 3.3 for more

details). In Appendix A, we summarize the full spectroscopic sample from MUSE.

### 3. DATA ANALYSIS

#### 3.1. Line Identification

We conduct a blind line search in the ALMA data cubes with the channel widths of 30 km s<sup>−1</sup> and 60 km s<sup>−1</sup>. First, we produce three-dimensional signal-to-noise ratio (S/N) cubes by dividing each channel with its standard deviation. Here we use the ALMA data cubes before the primary beam correction. We then search line candidates in the three-dimensional S/N cube by utilizing a python-base software of DENDROGRAM (Goodman et al. 2009) whose algorithm is similar to CLUMPFIND (Williams et al. 1994). In DENDROGRAM, we obtain an initial candidate catalog of line sources that meet the following criteria: at least 10 pixels and/or channels with a pixel value of  $\geq 2$  (i.e.,  $S/N \geq 2$ ). Performing the same procedure in the negative peaks in the S/N cubes under the assumption that the noise is Gaussian, DENDROGRAM evaluates the reliability of the initial line candidates based on the positive and negative properties of the peak S/N histograms, spatially integrated pixel values, and the channel width. This results in two reliable, bright line emitters both at  $\sim 268.7$  GHz.

We note that these two lines are also robustly identified with an independent blind line search method of González-López et al. (2017). Based on morphological, redshift, and gravitational lens properties of these two line emitters obtained in detail analyses in the following subsections (Section 3.2, 3.3, and 3.4), we refer to these two line emitters as  $z6.1/6.2$  ( $=z6.1$  and  $z6.2$ ) and  $z6.3$  throughout this paper.

In Figure 1, we present the ALMA spectra and the velocity-integrated intensity (i.e., moment 0) maps of  $z6.1/6.2$  and  $z6.3$ .  $z6.1/6.2$  shows an elongated morphology with two peaks in the moment 0 map. Although there is a possibility that a combination of the diffuse continuum and the noise fluctuation causes multiple peaks (e.g., Hodge et al. 2016), we confirm in Appendix B that the two peaks in  $z6.1/6.2$  are not caused by this combination through a realistic simulation. A single Gaussian fit to  $z6.1/6.2$  and  $z6.3$  in the line spectra is summarized in Table 1. Although we obtain consistent full-width-at-half-maximum (FWHM) values for the line widths between  $z6.1/6.2$  and  $z6.3$ , their frequency peaks are slightly different by  $69 \pm 22 \text{ km s}^{-1}$ . After integrating over a velocity range of  $1.5 \times \text{FWHM}$ ,  $z6.1/6.2$  and  $z6.3$  have S/N values of 9.2 and 8.0 at the peak pixels, respectively. A single elliptical Gaussian fit over a spatial area of  $6'' \times 6''$  in the velocity-integrated maps with the CASA task of IMFIT yields deconvolved spatial FWHM sizes of  $4''.24 \times 0''.82$  and  $1''.17 \times 0''.29$  for  $z6.1/6.2$  and  $z6.3$ , respectively. To obtain the integrated property, here we use a  $uv$ -tapered ( $1''.0 \times 1''.0$ ) map for  $z6.1/6.2$  in IMFIT. From line free channels, the continuum is also detected in the  $uv$ -tapered map ( $2''.0 \times 2''.0$ ) at  $4.5\sigma$  and  $2.5\sigma$  level from  $z6.1/6.2$  and  $z6.3$ , respectively. We also summarize the IMFIT results and the continuum flux density in Table 1. Further analyses for the continuum emission are presented in N. Laporte et al. (submitted).

### 3.2. Optical-NIR Counterparts

The bright lines of  $z6.1/6.2$  and  $z6.3$  at  $\sim 268.7 \text{ GHz}$  could be CO or [C II] (e.g., Decarli et al. 2020). To determine which line corresponds to  $z6.1/6.2$  and  $z6.3$ , we investigate their optical to near-infrared (NIR) properties. In the top panel of Figure 2, we show optical-NIR *HST* images around  $z6.1/6.2$  and  $z6.3$ . From the line peak positions, we identify clear counterparts in the optical-NIR images within a spatial offset of  $\sim 0''.1$  for both  $z6.1/6.2$  and  $z6.3$ . Both counterparts have a noticeable dropout feature blueward of  $\sim 1 \mu\text{m}$ , and the one near  $z6.1/6.2$  shows a highly elongated shape aligned with the elongated shape in the 268.684-GHz line. In the highly elongated object near  $z6.1/6.2$ , we identify a compact

source at the center whose optical-NIR color is distinct from the other parts of the elongated object and indicative of an overlapping foreground object by chance. We carefully model and subtract this foreground object (see Appendix C) to study the elongated object near  $z6.1/6.2$  in the following analysis. In the northeast from  $z6.3$ , we also identify a nearby compact object. This has a photometric redshift of  $0.50^{+0.05}_{-0.32}$  (Kokorev et al. in prep.), presumably one of the member galaxies of RXCJ0600-2007 ( $z = 0.43$ ), but does not affect the photometry of  $z6.3$ .

We conduct optical-NIR photometry and spectral energy distribution (SED) analyses for these counterparts. We perform the aperture photometry and summarize results in Table 2. The detail procedure of the aperture photometry is described in Appendix C. With the aperture photometry results, we conduct SED fitting using the EAZY code (Brammer et al. 2008)<sup>2</sup>. We fit the photometric flux densities and their uncertainties with linear combinations of templates derived following Brammer et al. (2008) but adopting Flexible Stellar Population Synthesis models as the basis (Conroy et al. 2009; Conroy & Gunn 2010). We adopt the dust attenuation law of Kriek & Conroy (2013) with  $\delta = 0$  (i.e., a Calzetti et al. 2000 shape with an additional 2175 Å dust feature).

In Figure 2, we show probability distributions of photometric redshifts for the optical-NIR counterparts of  $z6.1/6.2$  and  $z6.3$ . We find that  $z6.1/6.2$  and  $z6.3$  both have peak probabilities close to  $z = 6.0$ , in excellent agreement with the bright-line detection at  $\sim 268.7 \text{ GHz}$  if it is the [C II] 158  $\mu\text{m}$  line at  $z = 6.07$ . In this case, observed line luminosities  $L_{\text{line}}$  (i.e., without the correction of the lensing magnification) are estimated to be  $4.5 \pm 0.4 \times 10^9 L_{\odot}$  and  $2.3 \pm 0.2 \times 10^9 L_{\odot}$  for  $z6.1/6.2$  and  $z6.3$ , respectively. With a standard modified blackbody at  $z = 6$  with a peak dust temperature  $T_{\text{d}} = 38 \text{ K}$  (e.g., Faisst et al. 2020) and a dust emissivity index  $\beta_{\text{d}} = 1.8$  (e.g., Chapin et al. 2009; Planck Collaboration et al. 2011), we also obtain the observed values of rest-frame FIR luminosities  $L_{\text{FIR}}$  to be  $5.8 \pm 1.3 \times 10^{11} L_{\odot}$  and  $3.3 \pm 1.3 \times 10^{11} L_{\odot}$  and subsequently line to rest-frame FIR luminosity ratios to be  $7.8 \times 10^{-3}$  and  $6.8 \times 10^{-3}$ , for  $z6.1/6.2$  and  $z6.3$ , respectively. These ratios are consistent with the typical range of the [C II] line  $L_{\text{[CII]}}$  and  $L_{\text{FIR}}$  ratio ( $L_{\text{[CII]}}/L_{\text{FIR}}$ ) among local galaxies (e.g., Brauher et al. 2008; Díaz-Santos et al. 2013), which also supports the bright lines at  $\sim 268.7 \text{ GHz}$  being the [C II] line. Based on the source redshift at  $z = 6.07$ , we

<sup>2</sup> <http://github.com/gbrammer/ezay-py>

**Table 2.** Observed *HST* and IRAC photometry of the multiple images of RXCJ0600- $z_6$ 

ID	F606W ( $\mu\text{Jy}$ )	F814W ( $\mu\text{Jy}$ )	F105W ( $\mu\text{Jy}$ )	F125W ( $\mu\text{Jy}$ )	F140W ( $\mu\text{Jy}$ )	F160W ( $\mu\text{Jy}$ )	3.6 $\mu\text{m}$ ( $\mu\text{Jy}$ )	4.5 $\mu\text{m}$ ( $\mu\text{Jy}$ )
$z_{6.1/6.2}$ (arc)	< 0.07	$0.32 \pm 0.04$	$1.17 \pm 0.07$	$1.41 \pm 0.13$	$1.42 \pm 0.11$	$1.34 \pm 0.07$	$8.18 \pm 0.42$	$6.02 \pm 0.34$
$z_{6.3}$	$0.05 \pm 0.02$	$0.27 \pm 0.02$	$0.99 \pm 0.03$	$1.18 \pm 0.06$	$1.17 \pm 0.05$	$1.19 \pm 0.03$	$5.46 \pm 0.20$	$4.17 \pm 0.17$
$z_{6.4}$	< 0.02	$0.07 \pm 0.02$	$0.13 \pm 0.03$	$0.14 \pm 0.05$	$0.17 \pm 0.04$	$0.13 \pm 0.03$	< 0.59	< 0.46 <sup>†</sup>
$z_{6.5}$	< 0.02	$0.19 \pm 0.02$	$0.51 \pm 0.03$	$0.63 \pm 0.05$	$0.66 \pm 0.04$	$0.68 \pm 0.03$	$0.40 \pm 0.18$	$0.50 \pm 0.15$

NOTE— The photometry is performed with separate strategies for four lensed images to account for the crowded cluster field and varying degrees of extended source morphology (see Appendix C). For non-detection, we list the upper limit at the  $2\sigma$  level.

† We obtain  $0.34 \pm 0.23 \mu\text{Jy}$  which we replace the  $2\sigma$  upper limit.

also confirm that star-formation rate (SFR) estimates are consistent between the SED fitting with the dust attenuation correction and the summation of the rest-frame UV ( $L_{\text{UV}}$ ) and  $L_{\text{FIR}}$  following the work of Bell et al. (2005) scaled to the Chabrier IMF,

$$\text{SFR} [M_{\odot} \text{yr}^{-1}] = 1.09 \times 10^{-10} (L_{\text{FIR}} + 2.2L_{\text{UV}}). \quad (1)$$

Although the  $z_{6.3}$  solution shows a small non-zero probability of being at  $z \sim 1$ , we also identify a 3.6- $\mu\text{m}$  excess feature in both  $z_{6.1/6.2}$  and  $z_{6.3}$  which is often observed in  $z \sim 6$  galaxies due to the contamination of the strong [O III] $\lambda$ 5007 and  $\text{H}\beta$  lines (e.g., Roberts-Borsani et al. 2016; Harikane et al. 2018). Therefore, the high- $z$  solution at  $z \sim 6$  is likely favored. Other possibilities for the bright line along with the high- $z$  solution might be CO(16-15) at  $z = 5.85$  and CO(17-16) at  $z = 6.28$ . However, recent ALMA studies derive constraints on ratios of  $L_{\text{CO}(16-15)}/L_{\text{FIR}}$  and  $L_{\text{CO}(17-16)}/L_{\text{FIR}} \lesssim 3 \times 10^{-4}$  among luminous quasars at similar redshifts (Carniani et al. 2019). This indicates that  $L_{\text{line}}/L_{\text{FIR}}$  of  $z_{6.1/6.2}$  and  $z_{6.3}$  are nearly 1.5-dex higher than the typical range, strongly disfavoring the possibilities of CO(16-15) and CO(17-16) lines. We thus conclude that  $z_{6.1/6.2}$  and  $z_{6.3}$  are [C II] line emitters at  $z = 6.07$ . Note that we confirm that the [C II] line solution is further supported by the lens models, intrinsic physical properties (see Section 3.4 and 3.5), and follow-up Gemini/GMOS spectroscopy (N. Laporte et al. submitted).

Based on the redshift of  $z = 6.07$ , we also examine the Ly $\alpha$  line in the MUSE data cube around  $z_{6.1/6.2}$  and  $z_{6.3}$ . We do not identify any Ly $\alpha$  features neither around  $z_{6.1/6.2}$  nor  $z_{6.3}$ . With the rest-frame UV luminosity, this provides  $3\sigma$  upper limits of the Ly $\alpha$  equivalent width ( $EW_{\text{Ly}\alpha}$ ) at 4.4  $\text{\AA}$  and 3.7  $\text{\AA}$  for  $z_{6.1/6.2}$  and  $z_{6.3}$ , respectively. Given the dust continuum detection and the redshift, the absence of the bright Ly $\alpha$  line would be ascribed to dust and/or neutral hydrogen in interstellar and intergalactic media. This emphasizes the importance of the ALMA blind line search which

enable studies of galaxies irrespective of their Ly $\alpha$  line properties in particular in the epoch of reionization.

### 3.3. Mass Model

To study intrinsic physical properties of the [C II] line emitters  $z_{6.1/6.2}$  and  $z_{6.3}$ , we construct several mass models for the galaxy cluster RXCJ0600-2007 ( $z = 0.430$ ), using independent algorithms including GLAFIC (Oguri 2010), LENSTOOL (Jullo et al. 2007), and Light-Traces-Mass (LTM; Zitrin et al. 2015). Multiple images are selected based on the morphology and colors of galaxies in the *HST* images taken with RELICS, guided by  $y$  mass models. These models also exploit the MUSE spectroscopic redshift catalog (see Section 2.2) for redshift information of some multiple image systems as well as secure identifications of cluster member galaxies. These models adopt nearly identical sets of multiple image systems for constructing the mass models and provide almost consistent predictions for multiple image positions and magnification factors. A brief summary of these mass models is also presented in N. Laporte et al. (submitted), while full details will be given in a separate paper (in preparation). In this paper, we adopt the mass model of GLAFIC as a fiducial model for our analyses and here describe its construction below, although we also use results of LENSTOOL and LTM models to evaluate uncertainties in magnification factors.

We construct the mass model with GLAFIC in the same manner as in Kawamata et al. (2016). Our mass model consists of cluster-scale halos and cluster member galaxies. We place the cluster-scale halos at the positions of the three brightest cluster member galaxies in the core of the cluster. The position of one of the three cluster-scale halos is treated as a free parameter, whereas those of the other two cluster-scale halos are fixed to the galaxy positions. The cluster-scale halos are modeled by an elliptical Navarro-Frenk-White (NFW; e.g., Navarro et al. 1997) profile. The cluster member galaxies are selected using both photometric redshifts of galaxies measured

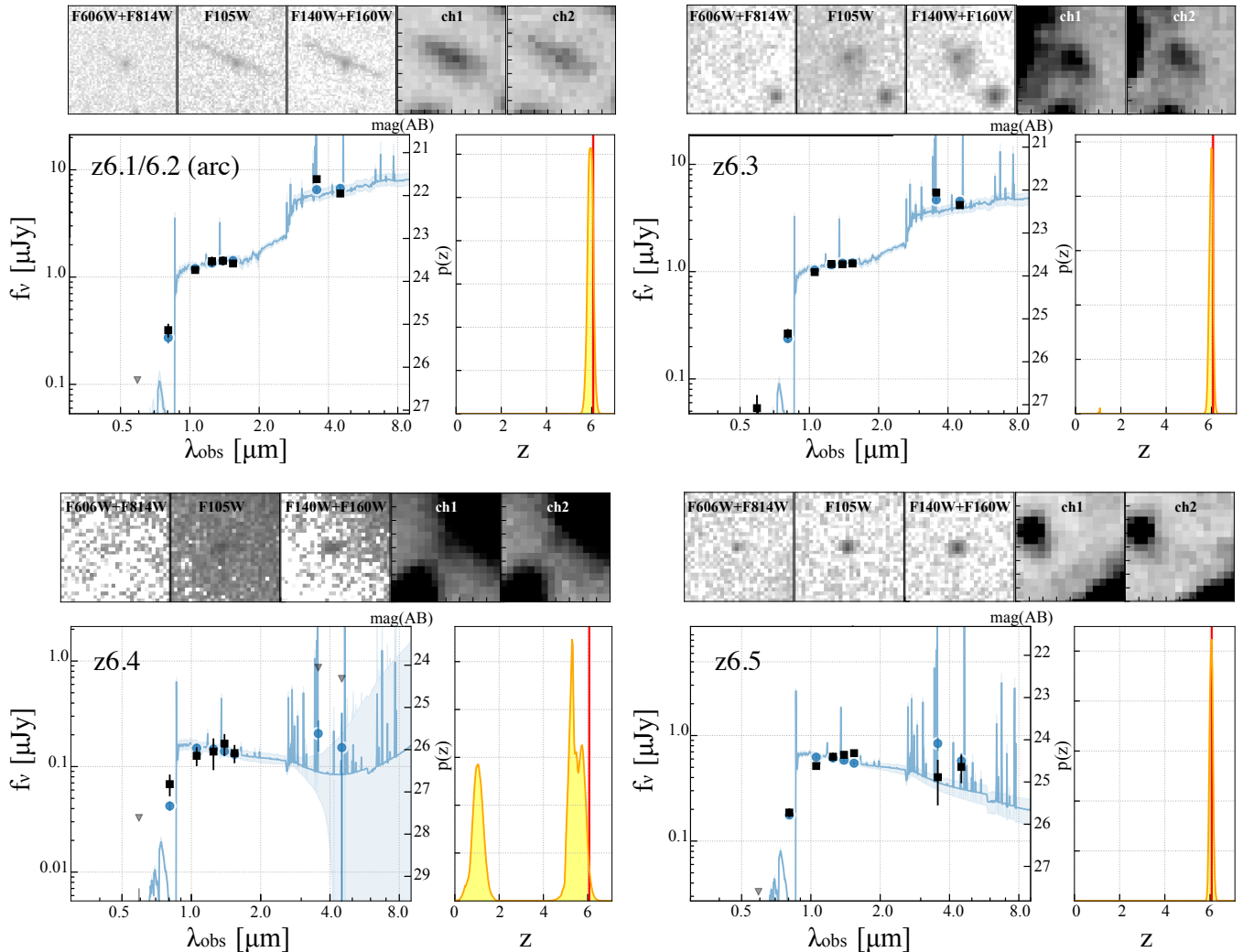


**Figure 2.** Observed optical-NIR properties of  $z6.1/6.2$ ,  $z6.3$ ,  $z6.4$ , and  $z6.5$  that are predicted as multiple images of a background LBG at  $z \sim 6$  consistently from different mass models (except for  $z6.5$  whose identification as a multiple image is tentative). **Top:** Cutouts of the *HST* ( $3'' \times 3''$ , except for  $z6.1/6.2$  with  $6'' \times 6''$ ) and *Spitzer* ( $8'' \times 8''$ ) images. Some of the *HST* images are integrated one. The filter name is presented at the top. **Bottom:** *HST* and *Spitzer* photometry (black square) and the best-fit templates, where gray triangles are the upper limits. The sum of individual EAZY templates is shown in the light blue curve. The yellow shaded region is the probability distribution of the photometric redshift  $p(z)$  from the SED fit. The red line indicates the spectroscopic redshift from the [C II] lines at  $\sim 268.7$  GHz. A  $3.6\text{-}\mu\text{m}$  excess feature in  $z6.1/6.2$  and  $z6.3$  is explained by the contamination of the strong [O III] $\lambda 5007$  and  $H\beta$  lines that are often observed in  $z \sim 6$  galaxies (e.g., Roberts-Borsani et al. 2016; Harikane et al. 2018).

from *HST* images (Coe et al. 2019) as well as galaxy colors. The position and shapes of the member galaxies are fixed to those derived from the *HST* image and treat their velocity dispersions and truncation radii using a pseudo-Jaffe ellipsoid as model parameters assuming a scaling relation (see Kawamata et al. 2016, for more details). In order to achieve a good fit, a member galaxy located at (R.A., Dec.)=(06:00:10.664,  $-20:06:50.65$ ) that produces multiple images is treated as a separate component, again assuming a pseudo-Jaffe ellipsoid. An external shear term, which provides a modest improvement of the mass modeling result, is also included in the mass

modeling of this cluster. After including the multiple images presented in Section 3.4 that are confirmed with help of our preliminary mass models, there are positions of 26 multiple images for eight sets of multiple image systems (five multiple image sets with spectroscopic redshifts) that we adopt as constraints. We optimize the parameters of the mass model based on a standard  $\chi^2$  minimization and determine the best-fit mass model assuming a positional error of  $0''.6$  for each multiple image to account for perturbations by substructures in the cluster that are not included in our mass model, and estimate the statistical error using the Markov-chain Monte

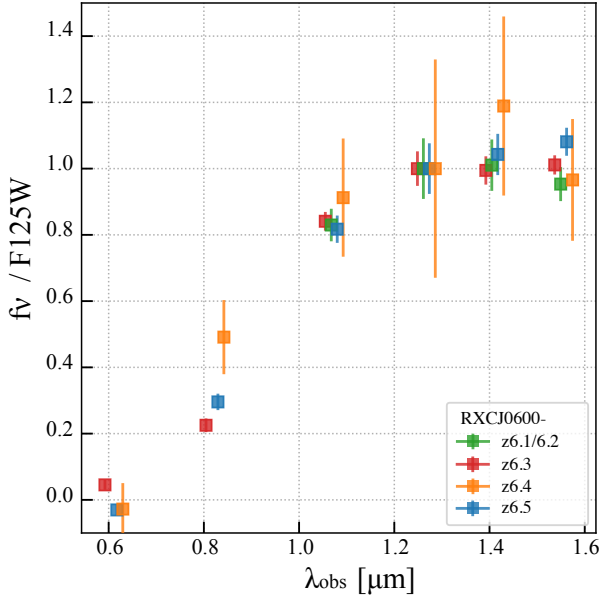


**Figure 3.** Observed SEDs of the multiple images of RXCJ0600- $z6$  in the *HST* bands normalized by the F125W band. The green, red, brown, and blue squares present  $z6.1/6.2$ ,  $z6.3$ ,  $z6.4$ , and  $z6.5$ , respectively.

Carlo method. Our best fitting model has  $\chi^2 = 20.0$  for 17 degree of freedom. Interested readers are referred to Kawamata et al. (2016) for more specific mass modeling procedures using GLAFIC.

Note that we do not include the foreground object overlapping  $z6.1/6.2$  in our mass models, because of the absence of its spectroscopic redshift. We will discuss the potential contribution of the foreground object to the morphology and magnification factor of  $z6.1/6.2$  in Section 4.1.

### 3.4. Multiple Images

From all of our mass models, we consistently obtain the following two predictions: i)  $z6.1/6.2$  consists of a pair of two multiple images of a galaxy at  $z \sim 6$  behind RXCJ0600-2007, and ii)  $z6.1/6.2$  and  $z6.3$  are also multiple images of the galaxy. The prediction of ii) is consistent with the [C II] morphology that has two close peaks. In fact, we confirm in Appendix D that [C II] line spectra produced at these two peaks show line profiles consistent with each other. In addition, almost the same optical-NIR SED shapes between  $z6.1/6.2$  and  $z6.3$  in Figure 2 support the prediction of ii). Although we identify the slight velocity shift between  $z6.1/6.2$  and  $z6.3$  by  $69 \pm 22 \text{ km s}^{-1}$  (see Section 3.1), the offset is much smaller than the typical FWHM range of the [C II] line among  $z \sim 4-6$  galaxies evaluated in the ALPINE survey ( $\sim 120-380 \text{ km s}^{-1}$ ; Béthermin et al. 2020), suggesting that the slight velocity shift is explained by the differ-

ential magnification at different regions of the galaxy. We thus interpret  $z6.1/6.2$  and  $z6.3$  as multiple images of the [C II] line emission at  $z = 6.07$  from a Lyman-break galaxy (LBG) behind RXCJ0600-2007. Hereafter we refer to the background LBG as RXCJ0600- $z6$ .

Subsequently, the different models also predict two additional multiple images of RXCJ0600- $z6$ , the positions of which we present in Figure 1, where we identify corresponding optical-NIR objects. We refer to these potential multiple images as  $z6.4$  and  $z6.5$ . Note that different mass models predict a consistent position for  $z6.4$ , while they predict different positions for  $z6.5$  with a scatter in a  $\sim 12''$  scale. In this paper, we focus an optical-NIR object as  $z6.5$  predicted by one of our mass models, but it should be regarded as tentative, as we will discuss below.

To investigate whether multi-wavelength properties of these potential multiple images are similar to  $z6.1/6.2$  and  $z6.3$ , we conduct the aperture photometry for  $z6.4$  and  $z6.5$  in the optical-NIR bands. The detail procedure of the aperture photometry is again described in Appendix C. In Table 2 and Figure 3, we summarize the photometry results and the optical-NIR colors normalized by the photometry at the F125W band, respectively. We find that  $z6.4$  and  $z6.5$  have similar optical-NIR SEDs with  $z6.1/6.2$ ,  $z6.3$  within the errors, consistent with our mass model predictions as multiple images at  $z \sim 6$ . We further perform the optical-NIR SED fitting to  $z6.4$  and  $z6.5$  in the same manner as  $z6.1/6.2$  and  $z6.3$ . In Figure 2, we also show the optical-NIR SED fitting results of  $z6.4$  and  $z6.5$ . While the  $z6.4$  photometry also allows for a  $z \sim 6$  solution, the possibility of much lower redshifts cannot be excluded due to the large uncertainties from its faint property and the potential contamination of the nearby BCG (see Appendix C.3).  $z6.5$  has a well-localized peak probability at  $z \sim 6$ , though the *HST-Spitzer* color of  $z6.5$  is much bluer than seen for the bright images  $z6.1/6.2$  and  $z6.3$ . In fact, an IRAC source at the location of  $z6.5$  should be easily detected if it has with the same color as those of the other images.

Because  $z6.4$  falls in the ALCS area coverage, we also examine whether the [C II] line emission is detected from  $z6.4$  with a frequency consistent with  $z6.1/6.2$  and  $z6.3$ . In Figure 1, we also show the ALMA Band 6 spectrum of  $z6.4$  based on an optimized aperture with a radius of  $1''.5$ . We find that  $z6.4$  has a tentative line detection ( $3.0\sigma$ ) at the consistent frequency with  $z6.1/6.2$  and  $z6.3$ . Moreover,  $z6.4$  has an asymmetry line profile (the brighter peak at the higher frequency side) which is consistent with the line profile of  $z6.3$ . These results strengthen

**Table 3.** Observed Physical Properties of the multiple images of RXCJ0600-z6

ID	$z_{\text{phot}}$	$z_{\text{spec}}$	$M_{\text{UV}}$ (mag)	SFR ( $M_{\odot} \text{ yr}^{-1}$ )	$M_{\text{star}}$ ( $\times 10^9 M_{\odot}$ )	$A_{\text{v}}$ (mag)	$\mu_{\text{whole}}^{\dagger}$	$\mu_{\text{local}}^{\dagger}$
z6.1/6.2 (arc)	$5.95_{-0.13}^{+0.11}$	$6.0734 \pm 0.0003$	$-23.23 \pm 0.07$	$135_{-23}^{+45}$	$41.9_{-10.1}^{+0.4}$	$0.07_{-0.05}^{+0.11}$	$29_{-7}^{+4}$	$163_{-13}^{+27}$
z6.3	$5.99_{-0.09}^{+0.07}$	$6.0719 \pm 0.0004$	$-23.06 \pm 0.06$	$114_{-26}^{+11}$	$20.1_{-2.7}^{+1.8}$	$0.18_{-0.11}^{+0.09}$	$21_{-7}^{+14}$	–
z6.4	$5.25_{-4.24}^{+0.48}$	(6.0719)	$-21.02 \pm 0.11$	$2.6_{-0.1}^{+1.2}$	$0.23_{-0.01}^{+0.12}$	$1.80_{-1.78}^{+2.25}$	$3.3_{-1.2}^{+2.4}$	–
z6.5	$6.05_{-0.07}^{+0.07}$	–	$-22.48 \pm 0.05$	$8.7_{-0.1}^{+0.7}$	$0.77_{-0.01}^{+0.05}$	$0.03_{-0.01}^{+0.12}$	$4.2_{-1.3}^{+1.8}$	–

NOTE— Physical properties obtained from the SED fitting of the observed photometry with EAZY without correcting for the lensing magnification. The intrinsic physical properties after the correction of the lensing magnification are summarized in Table 4. Based on the conversion from the UV and FIR luminosity of Bell et al. (2005) scaled to the Chabrier IMF, we obtain consistent SFR estimates of  $188 \pm 15 M_{\odot} \text{ yr}^{-1}$  and  $120 \pm 14 M_{\odot} \text{ yr}^{-1}$  for z6.1/6.2 and z6.3, respectively. Because the UV luminosity dominates in both z6.1/6.2 and z6.3, a  $\pm 10$  K difference in the  $T_{\text{d}}$  assumption for the  $L_{\text{FIR}}$  calculation (Section 3.2) changes these SFR estimates by  $\sim 0.1$  dex.

<sup>†</sup> We define  $\mu_{\text{whole}}$  and  $\mu_{\text{local}}$  as follows:

$$\mu_{\text{whole}} = (\text{observed luminosity of the multiple image}) / (\text{overall luminosity of the intrinsic galaxy})$$

$\mu_{\text{local}} = (\text{observed luminosity of the multiple image}) / (\text{local luminosity of the strongly lensed, sub region near the caustic line})$ , where the sub region corresponds to the dashed rectangle area in Figure 4. The errors are evaluated from the minimum to maximum range among our independent mass models.

the case that z6.4 is indeed one of the multiple images of the background LBG.

Based on these results, we find that the identification of z6.4 as one of the multiple images is relatively secure from the consistent predictions of the mass models as well as the line detection at the consistent frequency. On the other hand, from the different predicted positions among different mass models and the disagreements in the *HST-Spitzer* color with other multiple images, the interpretation of z6.5 being another multiple image is not secure and should be taken with caution until a spectroscopic redshift is obtained in follow-up observations. We thus use the positions of z6.1/6.2, z6.3, and z6.4 as constraints in deriving our best-fit mass models. We present the critical curve at  $z = 6.07$  from the best-fit mass model of GLAFIC in the left panel of Figure 1. We summarize the [C II] line properties and the SED fitting results for all these multiple images in Table 1 and Table 3, respectively.

### 3.5. Physical Properties of RXCJ0600-z6

The configuration of the multiple images is helpful to obtain the precise information about the source position and its surface brightness profile in the source plane. Here we estimate the intrinsic two-dimensional (2D) surface brightness profile by fitting the *HST* images assuming the fiducial mass model. Specifically, we first produce a  $1''.7 \times 1''.7$  cutout *HST*/F160W image of z6.3. With a single Sérsic profile model in the source plane, we then obtain the best-fit effective radius  $r_e = 1.2_{-0.1}^{+4.1}$  kpc (major axis), axis ratio of  $0.49_{-0.02}^{+0.03}$ , position angle =  $84_{-2}^{+2^\circ}$ , Sérsic index  $n = 2.5_{-0.1}^{+1.2}$ , and central coordi-

nate of (RA, Decl.)=(6:00:08.12,  $-20:07:39.55$ ) based on standard  $\chi^2$  minimization. Because we find a degeneracy between  $r_e$  and  $n$ , here we restrict the Sérsic index to the range of  $1 < n < 4$  in the fitting. We do not use z6.1/6.2 and z6.4 for the fitting due to the complicated morphology and the contamination of the diffuse emission from the nearby BCG, respectively. We note that here we ignore the clumpy structure of z6.3 for the moment, which we will discuss later. We list these best-fit Sérsic profile results in Table 4.

In Figure 4, we show the best-fit 2D Sérsic profile in the source plane and its multiple images in the image plane. We find that a single Sérsic profile well reproduces not only z6.3, but also z6.4 and z6.1/6.2 whose elongated shape is interpreted as a result of the source crossing the caustic line in the source plane and stretched over  $\sim 6''$  scale in the image plane (e.g., Vanzella et al. 2020). This interpretation is consistent with the slight difference in the line peak frequencies and the line profiles between z6.1/6.2 and z6.3 (Section 3.1), because the sub region of the galaxy can have different kinematics properties compared to the whole galaxy. By calculating the ratio of the spatial areas between the source and image planes, the magnification factors for z6.1/6.2 and z6.3 in our fiducial model (average of the three independent models) are estimated to be  $\sim 150$  (163) and  $\sim 35$  (21), respectively. The observed luminosity of z6.1/6.2 is 33 (29) times brighter than the intrinsic overall luminosity of RXCJ0600-z6 due to the strong gravitational lensing effect near the caustic line. By comparing physical properties of z6.3 and z6.4 that are both tracing the whole region of the lensed galaxy,

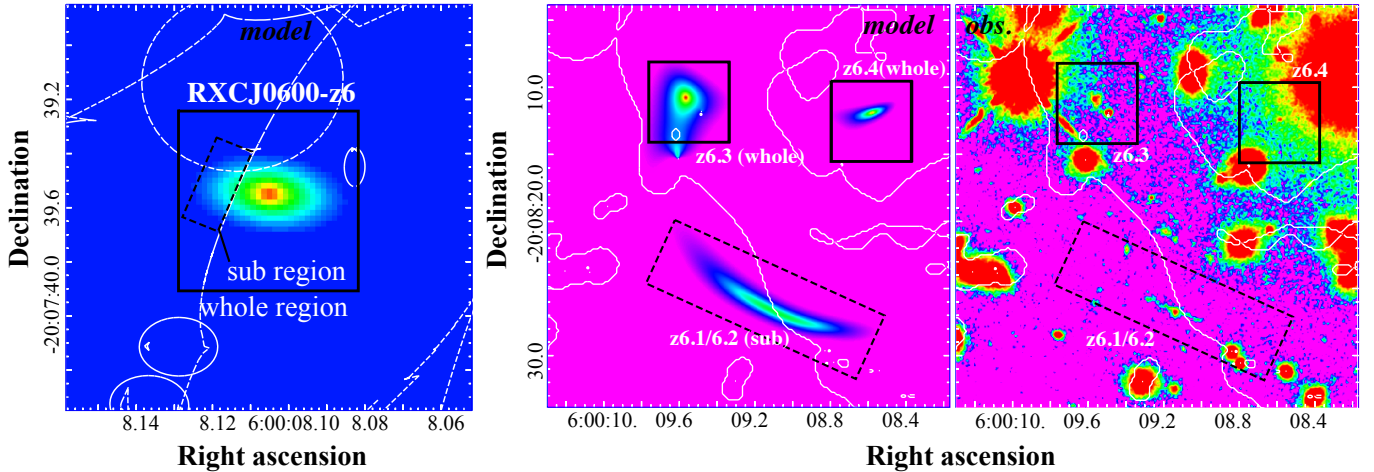


**Figure 4.** **Left:** The best-fit 2D Sérsic profile (effective radius in major axis = 1.2 kpc, axis ratio = 0.49, Sérsic index  $n = 2.5$ ) and coordinate (R.A., Decl. = 6:00:08.12,  $-20:07:39.55$ ) of the lensed LBG RXCJ0600- $z6$  at  $z = 6.0719$  in the source plane based on the fiducial mass model. The fitting is performed based on the standard  $\chi^2$  minimization only with the  $1''.7 \times 1''.7$  *HST*/F160W cutout of  $z6.3$ . The white dashed curves denote the caustic lines at the source redshift. **Middle:** The multiple images of RXCJ0600- $z6$  in the image plane,  $z6.1/6.2$ ,  $z6.3$ , and  $z6.4$ , predicted by the fiducial mass model with the best-fit 2D Sérsic profile in the left panel. The black boxes show the  $6'' \times 6''$  areas around  $z6.3$  and  $z6.4$  at the same positions as the yellow boxes in Figure 1. The dashed black rectangle denotes the  $6'' \times 17''$  area around  $z6.1/6.2$ , which approximately corresponds to the dashed black rectangle shown in the left panel along the caustic line. The white line indicate the critical curve. **Right:** The *HST*/F160W image showing the multiple images of  $z6.1/6.2$ ,  $z6.3$ , and  $z6.4$ . The image size is the same as the middle panel. The color and symbols are assigned in the same manner as the middle panel.

we confirm that our independent mass models agree in the ratio of magnification factors between  $z6.3$  and  $z6.4$  in the range of 6.1–6.7, which is consistent with the observed  $L_{[\text{CII}]}$  ratio of  $5.7 \pm 2.7$  between  $z6.3$  and  $z6.4$ . These results validates our best-fit mass models and 2D Sérsic profile in the source plane.

To be conservative, we adopt the average value of the magnification factors and evaluate its uncertainty from the minimum to maximum values among our independent mass models, when we estimate the intrinsic physical properties of RXCJ0600- $z6$  in this paper. We list the average magnification factor and its uncertainty in Table 3. Applying the average magnification factors to the FIR (Section 3.1) and optical-NIR (Section 3.2) properties, we summarize the intrinsic physical properties in whole and sub regions of RXCJ0600- $z6$  in Table 4. Remarkably, we obtain the intrinsic absolute rest-frame UV magnitude of  $M_{\text{UV}} = -19.75^{+0.55}_{-0.45}$ , which is  $\sim 3$  times fainter than  $L^*$  of the LBG luminosity function at  $z = 6$  ( $M_{\text{UV}} = 20.91^{+0.07}_{-0.06}$ ; Ono et al. 2018). In Figure 5, we show the SFR and  $M_{\text{star}}$  relation of RXCJ0600- $z6$ . For comparison, we also present the average relation among  $z \sim 6$  galaxies estimated in Iyer et al. (2018) (gray shaded region). We find that RXCJ0600- $z6$  falls on the average relation from the sub to whole regions. We also find that the relation between the [C II] line width and luminosity in RXCJ0600- $z6$  agrees with the average value among  $z \sim 6$  galaxies and the theoretical

prediction (see Figure 10 in Kohandel et al. 2019). The circularized effective radius ( $r_{\text{e,circ}} \equiv r_{\text{e}} \times \sqrt{\text{axis ratio}}$ ) of 0.84 kpc also falls in a typical range among  $z \sim 6$  galaxies with the similar UV luminosity (see e.g., Figure 9 of Kawamata et al. 2018). These results indicate that RXCJ0600- $z6$  is an abundant, representative sub- $L^*$  galaxy at this epoch. We note that these intrinsic physical properties are consistent with independent estimates in N. Laporte et al. (submitted) within the errors, even though the SED fitting strategies are different due to the different scopes in the paper.

#### 4. [C II] VIEWS FROM ISM TO COSMIC SCALES

The uniquely and strongly lensed galaxy near the caustic line (Section 3.3) allows us to study ISM properties from internal to whole scales of the host galaxy. For an example of the whole view of the galaxy based on  $z6.3$ , the spatial resolutions of the HST map of  $\sim 0''.2$  translate into  $0''.04$  (corresponding to  $\sim 250$  pc at  $z = 6.07$ ) after the correction of the lensing magnification, providing sub-kpc scale ISM views. At the same time, the blind aspect of the ALCS survey also allows us to statistically evaluate the number density of the [C II] line emitters at  $z \sim 6$  in a cosmic scale based on our successful identification of RXCJ0600- $z6$ . In conjunction with the rest-frame UV and FIR continuum properties, we examine the [C II] line properties from the ISM to cosmic scales and discuss whether there is com-

**Table 4.** Intrinsic physical properties of strongly lensed LBG of RXCJ0600-z6

RXCJ0600-z6		
Name	Whole	Sub
Region	Whole	Sub
Counter image	z6.3	z6.1/6.2
	(1)	(2)
RA	06:00:08.11	06:00:08.13
Decl.	-20:07:39.65	-20:07:39.53
$z_{\text{spec}}$	$6.0719 \pm 0.0004$	$6.0734 \pm 0.0003^\dagger$
$\text{EW}_{Ly\alpha}^{\text{rest}}$ [Å]	< 4.4	< 3.7
$L_{[\text{CII}]}$ [ $\times 10^8 L_\odot$ ]	$1.1^{+0.7}_{-0.5}$	$0.3^{+0.1}_{-0.1}$
$M_{\text{UV}}$ [mag]	$-19.75^{+0.55}_{-0.44}$	$-17.70^{+0.17}_{-0.09}$
SFR [ $M_\odot \text{ yr}^{-1}$ ]	$5.4^{+4.5}_{-2.9}$	$0.8^{+0.4}_{-0.2}$
$M_{\text{star}}$ [ $\times 10^8 M_\odot$ ]	$9.6^{+6.0}_{-4.6}$	$2.6^{+0.2}_{-1.0}$
$A_v$ [mag]	$0.18^{+0.09}_{-0.11}$	$0.07^{+0.11}_{-0.05}$
$r_e$ [kpc]	$1.2^{+4.1}_{-0.1}$	–
$n$	$2.5^{+1.2}_{-0.1}$	–
axis ratio	$0.49^{+0.03}_{-0.02}$	–
PA [°]	$84^{+2}_{-2}$	–
$M_{\text{dyn}}$ [ $\times 10^9 M_\odot$ ]	$3 \pm 1$	–
$M_{\text{gas}}$ [ $\times 10^9 M_\odot$ ]	$2 \pm 1$	–
$f_{\text{gas}}$ [%]	$\sim 50\text{--}80$	–

NOTE— (1) The physical properties related to the whole region of the galaxy that we obtain by applying  $\mu_{\text{whole}}$  (Table 3) to the observed properties of z6.3. The best-fit Sérsic profile ( $r_e$ ,  $n$ , and axis ratio) is not estimated by using  $\mu_{\text{whole}}$ , but by optimizing the intrinsic 2D surface brightness profile in the source plane to match the 2D surface brightness profile of z6.3 in the image plane with GLAFIC (see Section 3.5). The circularized effective radius is estimated to be  $0.8^{+2.9}_{-0.1}$  kpc, which is consistent within  $\sim 1\text{--}2\sigma$  errors with an independent 2D surface brightness profile fit on the image plane in N. Laporte et al. (submitted). We calculate  $M_{\text{gas}}$  by subtracting  $M_{\text{star}}$  from  $M_{\text{dyn}}$ , which is consistent with another estimate from the empirical calibration with the [C II] luminosity (Zanella et al. 2018) of  $(3 \pm 1) \times 10^9 M_\odot$  (see Section 4.2). (2) The physical properties related to the local scale of the galaxy in the sub region near the caustic line, by applying  $\mu_{\text{local}}$  (Table 3) to the observed properties of z6.1/6.2. † The sub region is red-shifted by  $69 \pm 22 \text{ km s}^{-1}$ , which agrees well with the velocity gradient identified in the whole scale of RXCJ0600-z6 (see Section 4.2).

mon property or a large diversity among these multiple scales.

#### 4.1. Spatial Distributions of UV, FIR, and [C II] down to Sub-kpc Scale

Making full use of the gravitational lensing, we investigate spatial distributions of the [C II] line, rest-frame UV and FIR continuum on the source plane and com-

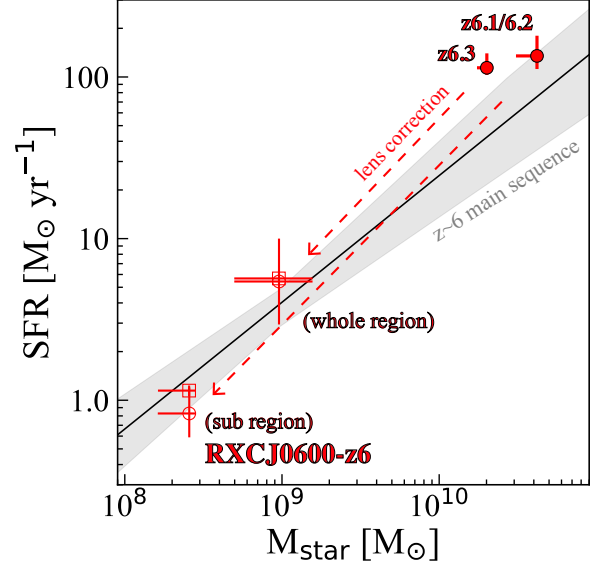


**Figure 5.** SFR- $M_{\text{star}}$  relation. The red filled and open circles indicate the relations before and after applying the correction of the lensing magnification to the SED fitting results, respectively, for z6.1/6.2 and z6.3. The errors include the uncertainty from the mass models (Table 3). The red open squares indicate SFR estimates after the lensing magnification correction based on the conversion from the UV and FIR luminosity of Bell et al. (2005) scaled to the Chabrier IMF. The black line and the gray shaded region denote the best-fit relation for  $z \sim 6$  galaxies and its  $1\sigma$  uncertainty evaluated in Iyer et al. (2018).

pare them. In the context of similar studies so far at  $z \sim 2\text{--}4$  for bright dusty, starburst galaxies (e.g., Swinbank et al. 2010, 2015; Dye et al. 2015; Spilker et al. 2016; Rybak et al. 2015; Tamura et al. 2015; Hatsukade et al. 2015; Rybak et al. 2020; Rizzo et al. 2020) and less massive galaxies (e.g., Dessauges-Zavadsky et al. 2017, 2019), this is a first observation to resolve the ISM structure down to the sub-kpc scale for the sub- $L^*$  galaxy in the epoch of reionization.

In the left panel of Figure 6, we present the rest-frame UV continuum maps for z6.3 (i.e., whole region) and z6.1/6.2 (i.e., sub region) taken in the *HST*/F160W band with the [C II] line (red contour) and the rest-frame FIR continuum (green contour) taken by ALMA. The emission peaks of the [C II] line and rest-frame FIR continuum are marked with the red and green squares (triangles) for z6.3 (z6.1/6.2) with the  $1\sigma$  error bars<sup>3</sup>, re-

<sup>3</sup> The error is estimated by the approximate positional accuracy of the ALMA map  $\Delta p$  in milliarcsec, given by  $\Delta p = 70000/(\nu * B * \sigma)$ , where  $\sigma$  is the peak SNR in the map,  $\nu$  is the observing frequency in GHz, and  $B$  is the maximum baseline length in kilometers (see Section 10.5.2 in cycle 7 ALMA technical handbook)

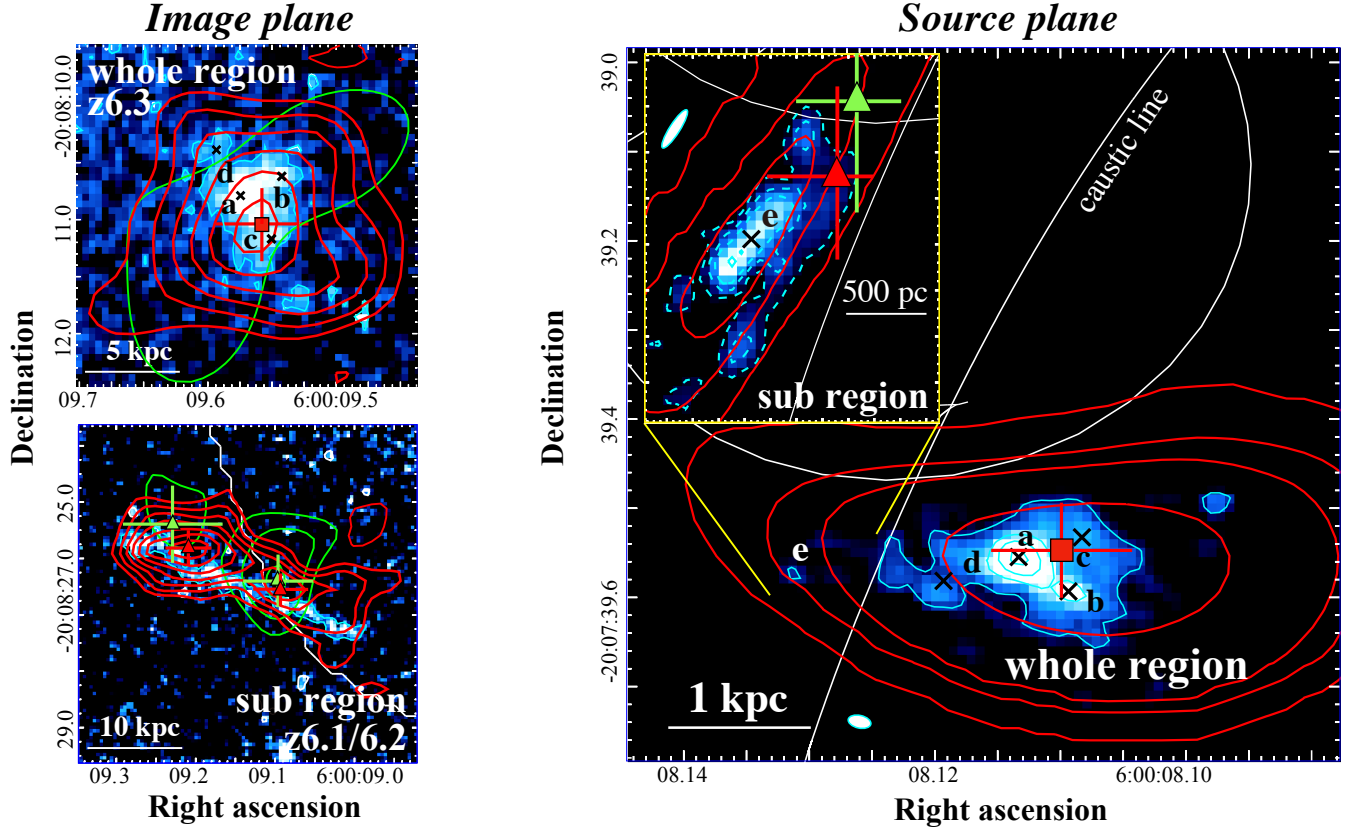


**Figure 6.** **Left:**  $3'' \times 3''$  and  $6'' \times 6''$  *HST*/F160W cutouts of  $z6.3$  (top) and  $z6.1/6.2$  (bottom) in the image plane. The small black crosses denote bright clumps (marked  $a$ ,  $b$ , and  $c$ ) and an elongated structure towards north east ( $d$ ) in the rest-frame UV continuum. The dashed black cross indicates the peak position of the rest-frame UV continuum after smoothing the *HST* map to match the resolution with ALMA. The red and green contours represent the [C II] line and the rest-frame FIR continuum from ALMA drawn at  $1\sigma$  intervals from  $2\sigma$  to  $8\sigma$ . The red and green squares (triangles) in  $z6.3$  ( $z6.1/6.2$ ) show the emission peak pixel positions of the [C II] line and rest-frame FIR continuum with the  $1\sigma$  error bars, respectively. The cyan contours are drawn at  $2\sigma$  for the rest-frame UV continuum. The foreground galaxies are removed with GALFIT for the source plane reconstruction. Here we use the natural-weighted map for the [C II] line, while the  $uv$ -tapered maps with  $2''.0 \times 2''.0$  and  $0''.8 \times 0''.8$  for the rest-frame FIR continuum of  $z6.3$  and  $z6.1/6.2$ , respectively. **Right:** Source plane reconstruction of the [C II] line and rest-frame UV and FIR continuum of  $z6.3$ . The color and symbols follow the same assignment as the left panel, where the cyan and red contours show 10%, 30%, 50%, and 80% of the peak. To match the spatial resolutions of ALMA and *HST*, the red contours are drawn from the source plane reconstruction of the de-convolved [C II] spatial distribution obtained with IMFIT (Section 3.1) that is smoothed with the *HST* PSF. The inset panel displays the source plane reconstruction of  $z6.1/6.2$ . The cyan (red) contours show 1%, 3%, 5%, and 10% (10%, 30%, and 50%) of the peak of the whole galaxy. The luminosity-weighted center is marked with label  $e$  which corresponds to the faint rest-frame UV clump at the western part of the whole galaxy. The white ellipses show the typical shape of the *HST* PSF reconstructed in the source plane. The error bars of the red square, triangle, and green triangle incorporate the average lensing magnification corrections and their uncertainties. Note that two peaks (= triangles) in  $z6.1/6.2$  in the image plane to be the multiple pair (Section 3.3), which thus correspond to one peak (= triangle) in the source plane.

spectively. Here we do not examine the rest-frame FIR continuum peak from  $z6.3$  due to the poor significance at the  $2.5\sigma$  level (see Section 3.1). In  $z6.3$ , the rest-frame UV continuum shows a clumpy structure, and thus we mark these clumps with black crosses labeled with  $a$ ,  $b$ , and  $c$ , from brightest to faintest. The rest-frame UV continuum of  $z6.3$  also shows an elongated structure toward the north east, which we mark with an additional black cross and label  $d$ . In  $z6.1/6.2$ , possible

clumps are more evident in the [C II] line and the rest-frame FIR continuum with the two-peak morphology. If RXCJ0600- $z6$  consists of a smooth disk, the morphology of  $z6.1/6.2$  would be a single smooth-arc shape as shown in the middle panel of Figure 4. Therefore, the two-peak morphology of  $z6.1/6.2$  may imply that the ISM of RXCJ0600- $z6$  near the caustic line has a clumpy structure in the source plane. An alternative possibility is that an intrinsically smooth disk is stretched into the

two-peak morphology in the image plane due to the perturbation by the foreground object overlapping  $z6.1/6.2$  which is not included in our fiducial mass model. To check this possibility, we include the foreground object in our mass model assuming that it is a member galaxy of the cluster (see Appendix C.2) and find that the two-peak structure can indeed be reproduced, if the mass associated with the foreground object is comparable or larger than that expected from the scaling relation of the luminosity and mass for cluster member galaxies constrained in our mass modeling. We conclude that we need more follow-up data including the spectroscopic redshift of the foreground object in order to discriminate these two possibilities. We however confirm that both magnification factors of  $\mu_{\text{local}}$  and  $\mu_{\text{whole}}$  for  $z6.1/6.2$  are affected only by  $\sim 1\text{--}2\%$  even if we include the foreground object in the mass model as one of the cluster members or outside of the cluster up to  $z \sim 4$ . The other foreground object near  $z6.3$  is classified as one of the member galaxies of the cluster (Section 3.2) and predicted to produce the critical curve at the southern east part of  $z6.3$  in our mass model (see the middle panel of Figure 4). However, we find that the [C II] morphology at the corresponding area is not disturbed at all, suggesting that its lensing effect is negligible for  $z6.3$ . We thus remove this foreground object from the mass model and the HST map with GALFIT in the source plane reconstruction of  $z6.3$ .

In the right panel of Figure 6, we present the source plane reconstruction of  $z6.3$  (whole region), where the inset panel displays the source plane reconstruction of  $z6.1/6.2$  (sub region). To match the spatial resolution between HST and ALMA, we create a [C II] map from the de-convolved [C II] spatial distribution (Section 3.1), smooth it with the point spread function (PSF) of the HST F160W band, and use this PSF-matched map for the source plane reconstruction of the [C II] line. In the right panel, the white ellipses indicate the source plane reconstruction of the HST PSF whose FWHM is decreased down to  $\sim 200 \times 100$  pc and  $\sim 300 \times 60$  pc around  $z6.3$  and  $z6.1/6.2$ , respectively. The other color and symbols follow the same assignment as the left panel, where we apply the lens correction also to the error bars. The error bar of the [C II] line peak position in  $z6.3$  (red square) is decreased down to  $\sim 300$  pc. These results indicate that we are able to map the ISM view down to a few hundred parsec scale. Note that our independent mass models consistently suggest that the two-peak morphology of  $z6.1/6.2$  in the image plane are the pair of multiple images (Section 3.3) regardless of whether there exists the foreground object or not, which thus correspond to one peak in the source

plane. We confirm that the entire morphology in both whole and sub regions of the galaxy and the emission peak positions does not change beyond the errors in the source plane whether we include or not the foreground galaxy overlapping  $z6.1/6.2$  in the mass model as one of the member galaxies of RXCJ0600-2007.

Firstly from the reconstruction of  $z6.3$ , we find on the scale of the galaxy that [C II] line peak shows an offset of  $\simeq 300$  pc from the brightest rest-frame UV clump of  $a$ , but they are consistent at the  $1\sigma$  error level. With the axis ratio of 0.49 (Table 4), non-parametric measurements directly on the surface brightness distributions in the source plane provide  $r_e = 1.1$  kpc and 2.6 kpc for the rest-frame UV continuum and the [C II] line emission, respectively, showing the spatially extended [C II] gas structure by a factor of  $\sim 2.4$ . These results are consistent with the recent ALMA results of Fujimoto et al. (2020b) for 23 individual normal star-forming galaxies at  $z \sim 4\text{--}6$ , whereby generally the [C II] line is spatially more extended than the rest-frame UV continuum by factors of  $\sim 2\text{--}3$  without a spatial offset beyond  $\simeq$  a 1-kpc scale. The  $r_e$  value for the rest-frame UV continuum is also consistent with the Sérsic profile fitting results of 1.2 kpc in the source plane presented in Section 3.5.

Secondly from the reconstruction of  $z6.1/6.2$ , we find in the sub region of the galaxy that the [C II] line is co-spatial with the rest-frame UV continuum again, which is separated by  $\sim 1.6$  kpc from the peak of the [C II] line and rest-frame UV continuum from the whole region of the galaxy. We mark the luminosity-weighted center of the sub region with the black cross labeled  $e$ . Remarkably, we find, in the independent rest-frame UV continuum map reconstructed from  $z6.3$ , that the faint clump exists exactly at the position of  $e$  whose peak flux density is also consistent. These agreements in the properties of the clump  $e$  also support the robustness of our best-fit mass models. We also find that the [C II] and rest-frame FIR peaks observed in the image plane are reconstructed in the source plane with a  $\simeq 1$  kpc offset from the luminosity-weighted center of  $e$ . This indicates that the faint diffuse emission or further faint clump near the caustic line is strongly lensed and more prominently visible in the image plane than the clump  $e$ . Given that RXCJ0600- $z6$  is quantified with  $r_e = 1.2$  kpc in the rest-frame UV continuum (Section 3.5), these results indicate that we are witnessing very faint [C II] and rest-frame FIR emitting region(s) near the caustic line beyond the effective radius of the galaxy that is almost invisible in other multiple images. Because of the poor significance level of the rest-frame FIR continuum in  $z6.3$ , we cannot conclude whether the rest-frame FIR continuum detected in  $z6.1/6.2$  corresponds to the

outskirt emission of the whole galaxy or the localized emission at the sub region of the galaxy.

Interestingly, the brightest peaks of the [C II] line and the rest-frame FIR continuum in  $z6.1/6.2$  appear on opposite sides in the image plane (Left bottom panel of Figure 6). In  $z6.1/6.2$ , the magnification factor is generally the same on either side. The clear difference identified in the [C II] line strength at the high significance levels ( $8.2\sigma$  and  $5.4\sigma$ ) suggests the existence of substructure of the mass distribution along the line-of-sight of  $z6.1/6.2$ , which is so-called *flux-ratio anomaly* (e.g., Mao & Schneider 1998). This is consistent with our interpretation that the central compact object in the optical-NIR bands in  $z6.1/6.2$  is the foreground object which is responsible for this *flux-ratio anomaly*. However, if the [C II] and rest-frame FIR emitting regions are identical in the source plane, the flux ratio should be the same between the [C II] and rest-frame FIR emission in the image plane. Although the current error bars of the spatial positions are large, this independent observable of the flux ratio suggests that the faint [C II] and rest-frame FIR emitting regions are physically offset in the sub region of RXCJ0600- $z6$ . This potential separation and the detailed ISM structure in RXCJ0600- $z6$  must be addressed in future deeper and higher-resolution observations.

#### 4.2. Kinematics via [C II]

We also examine the kinematics of RXCJ0600- $z6$  via the bright [C II] line emission. Here we focus on the [C II] kinematics of  $z6.3$  to characterize the gas kinematics of the whole galaxy. In the left panel of Figure 7, we present the velocity-integrated (top), velocity-weighted (middle), and velocity-dispersion (bottom) maps of  $z6.3$  in the image plane. We evaluate the root-mean-square noise level from the data cube and create these maps with a three-dimensional (3D) mask of all signal above the  $2\sigma$  level. We find that the [C II] line has the velocity gradient from  $-100$  to  $+45$   $\text{km s}^{-1}$  in east south to west north with its intensity extended up to a radius of  $\sim 1''.4$ . Assuming the line width estimate of  $z6.3$  (Table 1) and a potential error of  $\sim 30$   $\text{km s}^{-1}$  for the velocity gradient due to the spectral resolution of our ALMA data cube (Section 2.1), we obtain  $\Delta v_{\text{obs}}/2\sigma_{\text{tot}} = 0.94 \pm 0.26$ , where  $\Delta v_{\text{obs}}$  and  $\sigma_{\text{tot}}$  are the full observed velocity gradient (uncorrected for inclination) and the spatially-integrated velocity dispersion, respectively. With an approximate diagnostic for the classification of rotation-dominated and dispersion-dominated systems,  $\Delta v_{\text{obs}}/2\sigma_{\text{tot}} = 0.4$  (Förster Schreiber et al. 2009), we find that  $z6.3$  is classified as the rotation-dominated system. Note that

the beam smearing effect generally makes the velocity gradient [dispersion] underestimated [overestimated] in spatially low-resolution maps (see e.g., Figure 7 of Di Teodoro & Fraternali 2015). This strengthens the argument that  $z6.3$  is the rotation-dominated system from the increased  $\Delta v_{\text{obs}}/2\sigma_{\text{tot}}$  value without the beam smearing effect.

To study the rotation kinematics, we analyze our data in the image plane with softwares of  $3^{\text{D}}\text{BAROLO}$  (Di Teodoro & Fraternali 2015) and GALPAK3D (Bouché et al. 2015) that are tools for fitting 3D models to emission-line data cubes. In the left panel of Figure 7, we also show the best-fit 3D model and residual maps with  $3^{\text{D}}\text{BAROLO}$  by assuming three annuli for its tilted ring fitting algorithm. We find an excellent agreement on the intensity map and that the residual velocities in velocity-weighted and velocity-dispersion maps are generally less than the spectral resolution of our ALMA data cube ( $\sim 28$   $\text{km s}^{-1}$ ; Section 2.1). Although the residual in the velocity dispersion is relatively large near the edge of the mask, this is likely because the faint outskirts emission near the edge is masked in some velocity channels and the observed velocity dispersion is underestimated. These results suggest that the [C II] kinematics of  $z6.3$  is well reproduced by the best-fit 3D model. We confirm that an independent 3D modeling of a single exponential disk with GALPAK3D also provides the best-fit values of the rotation velocity, the velocity dispersion, and the inclination fully consistent within errors with the  $3^{\text{D}}\text{BAROLO}$  results. We summarize the details for the 3D modeling and the results in Appendix E.

In the middle panel, we present the velocity-weighted map of  $z6.3$  in the source plane via the reconstruction in the same manner as Section 4.1. To understand the intrinsic picture without the beam smearing effect, here we use the best-fit intrinsic (i.e., resolution free) map obtained from GALPAK3D for the reconstruction. In the right panel, we also show the [C II] radial velocity extracted from the three annuli with  $3^{\text{D}}\text{BAROLO}$  (black circle) as well as the best-fit (black line) and the  $1\sigma$  error (gray shade) of the rotation curve in the tanh formalization obtained from GALPAK3D. The correction the lensing magnification is applied to the radius scale. For comparison, the spatial and velocity offsets of  $z6.1/6.2$  are shown with the red triangle in both middle and right panels. We find that  $z6.1/6.2$  agrees with the velocity gradient of  $z6.3$  within the errors, which is consistent with our interpretation that  $z6.1/6.2$  is the sub region of RXCJ0600- $z6$ . This suggests that the clump  $e$  in the sub region of the galaxy (Section 4.1) is likely a small star-forming region within the rotation disk of the host galaxy.

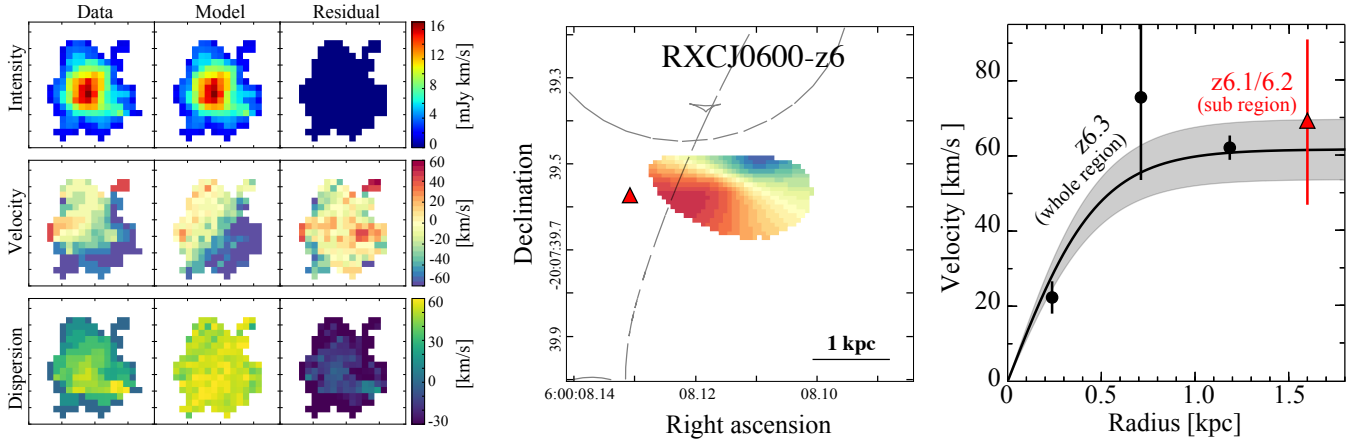


**Figure 7.** Kinematic properties of RXCJ0600-z6. **Left:** Velocity-integrated (i.e., intensity; top), velocity-weighted (middle), and velocity-dispersion (bottom) maps of z6.3 are shown in the left column. The best-fit 3D model with  $3^{\text{D}}\text{BAROLO}$  and the residual maps are presented in the middle and right columns, respectively. The image size is  $3'' \times 3''$ . **Middle:** Source-plane reconstruction of the intrinsic velocity-weighted map of z6.3 that was obtained with GALPAK3D. We limit the reconstruction up to the radius of  $1''.4$  from the [C II] intensity peak in the image plane. The grey dashed line is the caustic line. The red triangle shows the luminosity-weighted center of the sub region of the galaxy. **Right:** Observed radial velocity profile of z6.3 extracted from the three annuli defined for the  $3^{\text{D}}\text{BAROLO}$  analysis (black circles) and the spatial and velocity offsets of the sub region of the galaxy observed in z6.1/6.2 (red triangle). The black line shows the best-fit, together with the associate  $1\sigma$  error (grey shade), of the radial velocity profile of z6.3 obtained from GALPAK3D.

For the rotation-dominated system, we obtain the dynamical mass  $M_{\text{dyn}}$  of  $(3 \pm 1) \times 10^9 M_{\odot}$  based on an assumption of the disk-like gas potential distribution, following the equation (4) in Dessauges-Zavadsky et al. (2020)

$$\left(\frac{M_{\text{dyn}}}{M_{\odot}}\right) = 1.16 \times 10^5 \left(\frac{v_{\text{rot}}}{\text{km s}^{-1}}\right)^2 \left(\frac{r_e}{\text{kpc}}\right), \quad (2)$$

where  $v_{\text{rot}}$  is the rotation velocity of the gaseous disk after the inclination correction. We calculate the inclination from the axis ratio of the best-fit surface brightness profile results for the rest-frame UV continuum (Section 3.5), assuming that the higher-resolution map provides a better constrain for the inclination. We adopt  $r_e$  and  $v_{\text{rot}}$  from the source plane reconstruction of the [C II] line (Section 4.1) and the GALPAK3D results, respectively. We caution that the uncertainty of the inclination could remain by  $\sim 30\%$  even in the spatially resolved analysis (e.g., Rizzo et al. 2020), and thus the uncertainty in the above  $M_{\text{dyn}}$  estimate could be even larger. Given the negligible contribution of the dark matter halo in the galactic scale, we estimate the molecular gas mass  $M_{\text{gas}}$  to be  $\sim 1\text{--}2 \times 10^9 M_{\odot}$  by subtracting  $M_{\text{star}}$  (Section 3.5) from  $M_{\text{dyn}}$ . It is worth noting that this  $M_{\text{gas}}$  range agrees with another estimate based on an empirically calibrated method in Zanella et al. (2018), given by

$$\left(\frac{L_{[\text{CII}]}}{L_{\odot}}\right) = 10^{-1.28(\pm 0.21)} \times \left(\frac{M_{\text{gas}}}{M_{\odot}}\right)^{0.98(\pm 0.02)}, \quad (3)$$

which suggests  $M_{\text{gas}} = 3_{-1}^{+2} \times 10^9 M_{\odot}$ , despite the potentially large uncertainty of the inclination. These results indicate that RXCJ0600-z6 is a gas-rich galaxy with a high gas fraction of  $f_{\text{gas}} (\equiv M_{\text{gas}}/(M_{\text{star}} + M_{\text{gas}})) \sim 50\text{--}80\%$ . This is consistent with recent ALPINE results that [C II]-detected ALPINE galaxies with  $M_{\text{star}} \sim 1 \times 10^9 M_{\odot}$  have  $f_{\text{gas}} \sim 60\text{--}90\%$  (see Figure 8 in Dessauges-Zavadsky et al. 2020). These  $M_{\text{dyn}}$ ,  $M_{\text{gas}}$ , and  $f_{\text{gas}}$  estimates are also listed in Table 4.

Note that we cannot rule out the possibility that the velocity gradient is originally caused by complex dynamics with interacting, merging galaxies. Future higher resolution observations will confirm the smooth rotation of the disk or break the complex dynamics into the multiple components.

#### 4.3. SFR and $L_{[\text{CII}]}$ Relation

In the left panel of Figure 8, we show the relation between SFR and  $L_{[\text{CII}]}$  for z6.1/6.2 and z6.3. For comparison, we also show local and high-redshift galaxy results taken from the literature (Malhotra et al. 2001; Díaz-Santos et al. 2013; Magdis et al. 2014; De Looze et al. 2014; Herrera-Camus et al. 2015; Spilker et al. 2016; Cooke et al. 2018; Harikane et al. 2020; Matthee et al. 2019; Schaerer et al. 2020) and the  $L_{[\text{CII}]}$ -SFR relation obtained from local star-forming galaxies in De Looze et al. (2014). The observed  $L_{[\text{CII}]}$  of both z6.3 and z6.1/6.2 fall on the most luminous  $L_{[\text{CII}]}$  regime among typical (e.g.,  $\text{SFR} \lesssim 100 M_{\odot} \text{ yr}^{-1}$ ) high- $z$  star-forming galaxies, demonstrating the power of the gravitational

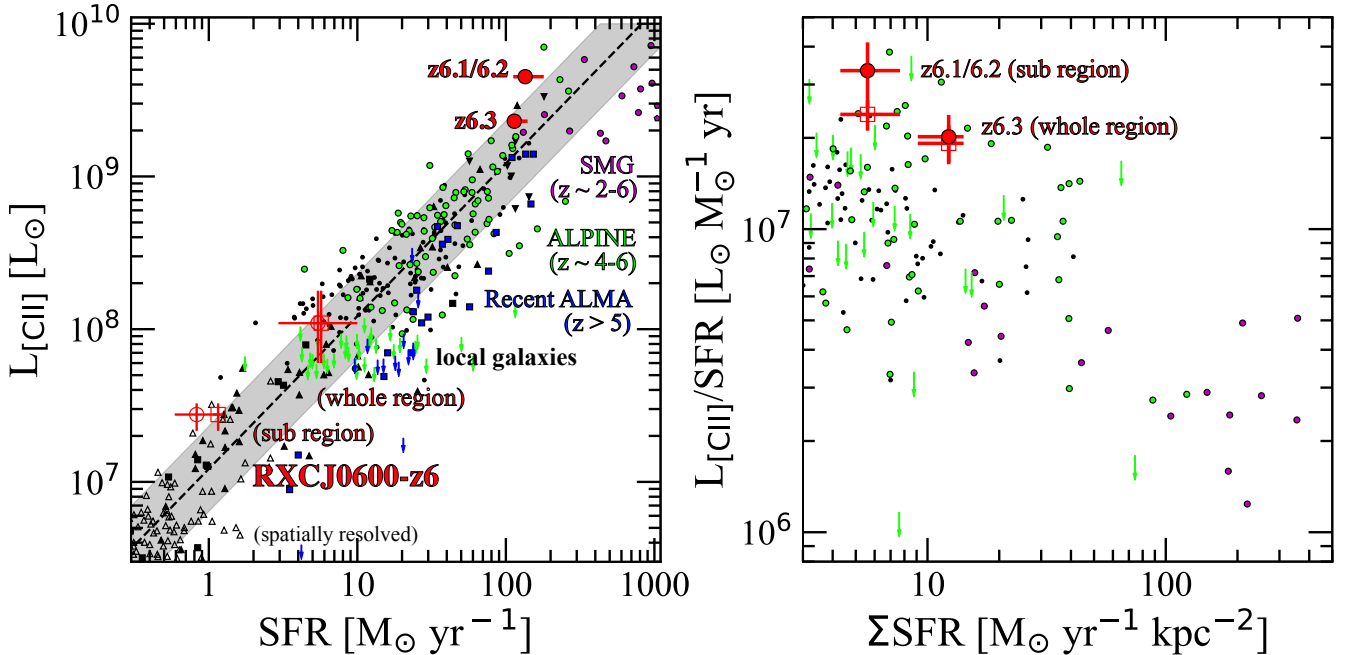


**Figure 8.** **Left:**  $L_{[\text{C II}]}$ –SFR relation. The red filled and open circles indicate  $z_{6.1/6.2}$  and  $z_{6.3}$  before and after the correction of the lensing magnification, respectively. The errors include the uncertainty from the mass models (Table 3). The red open squares indicate the SFR estimates after the correction of the lensing magnification based on the UV and FIR luminosity of Bell et al. (2005) scaled to the Chabrier IMF. The previous results from local to high- $z$  star-forming galaxies are shown with black circles (local LIRGs; Díaz-Santos et al. 2013), black squares (local dwarfs; De Looze et al. 2014), black triangles (local spirals; Malhotra et al. 2001), black inverse triangles ( $z \sim 0.3$  (U)LIRGs; Magdis et al. 2014), green circles ( $z \sim 4$ –6 star-forming galaxies from ALPINE; Schaerer et al. 2020), magenta pentagons ( $z \sim 5$  submillimeter galaxies (SMGs); Cooke et al. 2018), magenta circles ( $z \sim 2$ –6 lensed SMGs; Spilker et al. 2016), and blue squares (compilation of recent ALMA results for  $z > 5$  star-forming galaxies; Matthee et al. 2020 and Harikane et al. 2020). We adopt the average relation of the low- $z$  HII-galaxy/starburst sample from De Looze et al. (2014), which is adjusted to the Chabrier IMF by reducing the SFR by a factor of 1.06 in the same manner as Schaerer et al. (2020). The arrow indicates the  $3\sigma$  upper limit. The  $L_{\text{FIR}}$  value in the literature is firstly converted into a total IR luminosity  $L_{\text{TIR}}$  (8–1000  $\mu\text{m}$ ), and then we calculate SFR by using the calibration of Murphy et al. (2011). The spatially resolved results ( $\Sigma\text{SFR}$  and  $\Sigma L_{[\text{C II}]}$ ) for local galaxies are also presented with open triangles (Herrera-Camus et al. 2015) by assuming the area of 1  $\text{kpc}^2$ . The dashed line and gray shade denote the  $L_{[\text{C II}]}$ –SFR relation obtained from local star-forming galaxies (De Looze et al. 2014) and its dispersion, respectively. **Right:**  $L_{[\text{C II}]}/\text{SFR}$ – $\Sigma\text{SFR}$  relation. The color assignments on the symbols are the same as the left panel. We define the star-forming area by a circular area of the rest-frame UV emission with a radius of  $\sqrt{2} \times r_{\text{e,circ}}$  for the  $\Sigma$  SFR estimate. We use the factor of  $\sqrt{2}$  in accordance to Spilker et al. (2016). For  $z_{6.1/6.2}$  and  $z_{6.3}$ , we evaluate the rest-frame UV size by reducing the [C II] size measurements with IMFIT (Table 1) by a factor of 2 (Section 4.1). For the ALPINE sources, we use the rest-frame UV size measurement results in Fujimoto et al. (2020b). For local LIRGs and lensed SMGs, we use the rest-frame FIR size measurement results in Spilker et al. (2016) by assuming that the star-forming activity is dominated in the rest-frame FIR emitting regions in these objects.

lensing. After the correction of the lensing magnification, we find that both  $z_{6.3}$  and  $z_{6.1/6.2}$  fall slightly above, but still likely follow the SFR– $L_{[\text{C II}]}$  relation of the local galaxies within the dispersion. This is consistent with recent ALMA results that the average SFR– $L_{[\text{C II}]}$  relation among high-redshift star-forming galaxies at  $z \sim 4$ –9 is well within the intrinsic dispersion of the local relation (Carniani et al. 2018, 2020; Schaerer et al. 2020). Given that RXCJ0600- $z_6$  is consistent with being an abundant, sub- $L^*$  galaxy at  $z = 6$  (see Section 3.5), these results may suggest that the SFR– $L_{[\text{C II}]}$  relation, defined by local galaxies, holds from the spatially

resolved sub-kpc ISM to the whole scales in abundant galaxies even up to the epoch of reionization.

To further study the  $L_{[\text{C II}]}$ –SFR relation, the right panel of Figure 8 presents  $L_{[\text{C II}]}/\text{SFR}$  and SFR surface density ( $\Sigma\text{SFR}$ ). This relation or another relation between  $L_{[\text{C II}]}/L_{\text{FIR}}$  and  $L_{\text{FIR}}$  surface density ( $\Sigma L_{\text{FIR}}$ ) are known to have tight anti-correlations where the deficit of the [C II] line is explained by the high ionization state in the ISM around regions with high  $\Sigma\text{SFR}$  or  $\Sigma L_{\text{FIR}}$  (e.g., Díaz-Santos et al. 2013; Spilker et al. 2016; Gullberg et al. 2018; Ferrara et al. 2019). Importantly, these relations are not affected by the lensing magnification, be-

cause the same magnification factor applies to all these values. We find that  $z6.1/6.2$  shows a higher  $L_{[\text{C II}]}/\text{SFR}$  ratio, while both  $z6.1/6.2$  and  $z6.3$  are consistent with the trend of the anti-correlation. This indicates that the difference of  $\Sigma\text{SFR}$  causes the difference of the  $[\text{C II}]$  line luminosity at a given SFR between  $z6.1/6.2$  and  $z6.3$ , which is likely consistent with the source plane reconstruction results in Section 4.1: the faint  $[\text{C II}]$ -emitting region of  $z6.1/6.2$  is separated from the bright rest-frame UV clumps by  $\sim 1.6$  kpc in the source plane, where the ionization state of the local ISM is thought to be moderate.

We note that recent ALMA observations show non-detection results of the  $[\text{C II}]$  line from similarly star-forming galaxies at  $z \sim 4-9$  at the same time (see upper limits in Figure 8), indicative of the existence of galaxies whose  $L_{[\text{C II}]}-\text{SFR}$  relations are different from those of the local galaxies. Given the requirement of prior spectroscopic redshift with the  $\text{Ly}\alpha$  line in most cases (Section 3.2), those non-detections might be related to recent reports of the potential anti-correlation between  $L_{[\text{C II}]}/\text{SFR}$  and  $\text{EW}_{\text{Ly}\alpha}$  (Harikane et al. 2018, 2020; Carniani et al. 2018). In contrast to the most cases, RXCJ0600- $z6$  is identified in the blind survey and its physical properties (rest-frame  $\text{EW}_{\text{Ly}\alpha} < 4.4 \text{ \AA}$ ) agrees with the potential anti-correlation reported in Harikane et al. (2018). Another lensed galaxy at  $z = 6.15$  (Calura et al. 2021) also follows the similar trend with relatively large rest-frame  $\text{EW}_{\text{Ly}\alpha}$  ( $60 \pm 8 \text{ \AA}$ ) and small  $L_{[\text{C II}]}/\text{SFR}$  ( $\sim 2 \times 10^5$ ). A caution still remains that Schaerer et al. (2020) report a weak dependence of  $L_{[\text{C II}]}/\text{SFR}$  of  $\text{EW}_{\text{Ly}\alpha}$ . Since the  $[\text{C II}]$  line emissivity depends on the ISM properties such as the ionization state, metallicity, and gas density (e.g., Vallini et al. 2015), the different  $L_{[\text{C II}]}-\text{SFR}$  relations could be alternatively explained by a larger dispersion of the ISM properties in high- $z$  galaxies than in local galaxies. The uncertainties of the SFR estimates might contribute to the large dispersion in high- $z$  galaxies due to assumptions of the star-formation history, the dust-attenuation curve, and the stellar population age as discussed in Carniani et al. (2020) and Schaerer et al. (2020). Another recent reports of the extended  $[\text{C II}]$  line morphology up to a radius of  $\sim 10$  kpc (e.g., Fujimoto et al. 2019, 2020b; Ginolfi et al. 2020; Novak et al. 2020) might be also related to some of those non-detections, because the surface brightness of the extended emission is significantly decreased in relatively high-resolution maps (Carniani et al. 2020). Based on the visibility-based stacking, the secondary extended component up to the 10-kpc scale is estimated to have the average contribution to the total line luminosity of  $\sim 50 \%$  around star-forming galax-

ies (Fujimoto et al. 2019) and  $\sim 20\%$  around quasars (Novak et al. 2020) at  $z \sim 6$ . These non-negligible contributions could matter if the request sensitivity is close to the detection limit around the  $5\sigma$  level. However, this is not the case if the carbon in the extended  $[\text{C II}]$  gas is ionized by such as the gravitational energy in the cold stream, the shock heating in the outflow and/or inflow gas, and the AGN feedback, instead of the photoionization powered from the star-forming regions (see e.g., Section 5 of Fujimoto et al. 2019).

#### 4.4. $[\text{C II}]$ Luminosity Function

A key goal of ALCS is to constrain the number density of the line emitters. Although the complete blind line survey results with all 33 fields will be presented in a separate paper (in preparation), we can evaluate a lower limit of the  $[\text{C II}]$  luminosity function at  $z \sim 6$  with our  $[\text{C II}]$  line detection from the strongly lensed LBG at  $z = 6.0719$ .

To do this, we first measure the effective survey area using mass models for all 33 ALCS clusters at  $z \sim 6$  constructed in the same manner as described in Section 3.3. After the correction of the lensing magnification, we obtain an effective survey area of  $\sim 49$  (2) arcmin<sup>2</sup> at  $L_{[\text{C II}]} = 1.0 \times 10^9$  ( $10^8$ )  $L_{\odot}$ , assuming the line width of  $\text{FWHM} = 200 \text{ km s}^{-1}$  with the  $5\sigma$  detection limit. We then convert the effective survey area to the survey volume, based on the frequency setup in the ALCS observations covering the  $[\text{C II}]$  line emission at  $z = 5.974-6.172$  and  $6.381-6.602$ , and derive a lower limit of the  $[\text{C II}]$  luminosity function at  $z = 6$ .

In Figure 9, we present the number density of  $[\text{C II}]$  line emitters at  $z = 6$ , including recent  $[\text{C II}]$  line studies at  $z > 4$  (Swinbank et al. 2012; Matsuda et al. 2015; Yamaguchi et al. 2017; Cooke et al. 2018; Hayatsu et al. 2019; Yan et al. 2020; Decarli et al. 2020). For comparison, we also present  $[\text{C II}]$  luminosity functions from semi-analytical models (Popping et al. 2016; Lagache et al. 2018) and from the observed SFR function (SFRF; Smit et al. 2016) of optically-selected galaxies. For the conversion from SFRF to  $[\text{C II}]$  luminosity function, we adopt the  $[\text{C II}]-\text{SFR}$  relation of the local star-forming galaxies estimated in De Looze et al. (2014). We find that our lower limit estimate is consistent with both the semi-analytical results and SFRF. Note that we do not apply any completeness corrections to our lower limit estimate. The incompleteness for strongly lensed sources with large spatial sizes is generally significant due to its low surface brightness (e.g., Bouwens et al. 2017; Kawamata et al. 2018; Fujimoto et al. 2017). Although the incompleteness largely depends on the assumption of the intrinsic source size, this may indicate that the lower

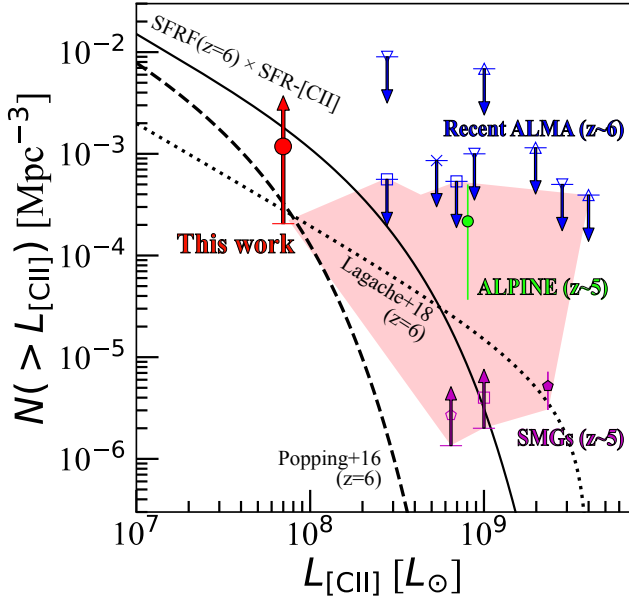


**Figure 9.** Cumulative [C II] luminosity function at  $z = 6$  with recent [C II] line studies at  $z > 4$ . The red circle shows the number density of the [C II] line emitter based on our successful detection from the strongly lensed LBG with the effective survey volume of the full ALCS data cubes composed of 33 galaxy clusters. The lower limit is estimated from the Poisson uncertainty at the single-sided confidence level of 84.13% presented in Gehrels (1986). Recent ALMA blind line survey results are presented with blue triangle (243 archival data cubes; Matsuda et al. 2015), blue inverse triangle (four massive galaxy clusters; Yamaguchi et al. 2017), blue square (ASPECS; Decarli et al. 2020), and blue cross (SSA22; Hayatsu et al. 2017, 2019). The green circle presents the ALPINE results (Loiacono et al. 2020; Yan et al. 2020). Here we show only the estimate from the serendipitous [C II] line detection at  $z \sim 5$  whose redshift is sufficiently separated from (i.e., not associated with) the central ALPINE targets. The magenta square and pentagon show the serendipitous [C II] line detection from bright SMGs at  $z \sim 5$  reported in Swinbank et al. (2012) and Cooke et al. (2018), respectively. The red shade indicates the current constraints based on our and previous results so far obtained. For comparison, we also present semi-analytical model results (Popping et al. 2016; Lagache et al. 2018) and SFR function (SFRF; Smit et al. 2016), including the dust correction based on the SMC extinction law, whose SFR value is converted into  $L_{[\text{C II}]}$  with the local [C II]–SFR relation (De Looze et al. 2014).

limit could be placed still higher and that the faint-end of the [C II] luminosity function might be close to SFRF. Indeed, other constraints from the recent [C II] line studies are also consistent with SFRF at the bright regime ( $L_{[\text{C II}]} \gtrsim 10^{8.5} L_{\odot}$ ). Although the brightest-end ( $L_{[\text{C II}]} \gtrsim 10^{9.2} L_{\odot}$ ) of SFRF is smaller than the constraints obtained from the SMG studies (Cooke et al. 2018), this is explained by the absence of such dusty-

obscured galaxies in the SFRF based on the optically-selected galaxies. Therefore, the constraints of the [C II] luminosity function so far obtained are likely consistent with the prediction from the local SFR– $L_{[\text{C II}]}$  relation and the SFRF at  $z = 6$ .

#### 4.5. From ISM to Cosmic Scales

The source plane reconstruction in Section 4.1 unveils the ISM structure down to a few hundred parsec scales, where we find that [C II] line is not displaced beyond a  $\sim 300$ -pc from the rest-frame UV continuum from the spatially resolved ISM to the whole galaxy. In Section 4.3, we find that the SFR– $L_{[\text{C II}]}$  relations from the spatially resolved ISM to the whole galaxy are consistent with those of local galaxies. In Section 4.4, we obtain the lower limit at the faintest regime of the  $z = 6$  [C II] luminosity function. We find that the prediction from the  $z = 6$  SFR function and the SFR– $L_{[\text{C II}]}$  relation of the local galaxies is consistent with our and previous constraints on the  $z = 6$  [C II] luminosity function in the wide  $L_{[\text{C II}]}$  range. Given the unbiased aspect of the ALCS survey and indeed the representative physical properties of RXCJ0600- $z6$  among the abundant population of the low-mass regime of  $z \sim 6$  star-forming galaxies (Section 3.5), our results may imply that the SFR– $L_{[\text{C II}]}$  relation of local star-forming galaxies is universal for a wide range of scales including the spatially resolved ISM, the whole region of the galaxy, and the cosmic scale.

## 5. SUMMARY

In this paper, we present the blind detection of a multiply-imaged line emitter behind the massive galaxy cluster RXCJ0600–2007 in a cycle-6 ALMA large project of ALMA Lensing Cluster Survey (ALCS). The optical–NIR property and our lens model analyses suggest that the emission line is the [C II] 158  $\mu\text{m}$  line from a Lyman-break galaxy (LBG) at  $z = 6.0719 \pm 0.0004$  behind RXCJ0600–2007. We study the relation between the star-formation rate (SFR) and [C II] line luminosity ( $L_{[\text{C II}]}$ ), the morphology, and the kinematics in the spatially resolved interstellar medium (ISM) as well as the whole scale of the LBG, and provide a lower limit at the faint-end of the [C II] luminosity function at  $z \sim 6$ , with help of the gravitational lensing magnification. The main findings of this paper are summarized as follows:

1. We perform blind line search for the ALCS data cube in RXCJ0600–2007 and identify two bright lines at  $\geq 8\sigma$  levels at  $268.682 \pm 0.011$  GHz and  $268.744 \pm 0.016$  GHz, one of which shows a strongly lensed arc shape. Both lines have optical–NIR counterparts with clear Lyman-break feature

- at  $\sim 9000 \text{ \AA}$ , indicative of the lines corresponding to the [C II]  $158 \mu\text{m}$  at  $z = 6.07$ . The optical–NIR spectral energy distribution (SED) analysis shows that probability distributions of their photometric redshifts are in excellent agreement with the [C II] line redshift, while other possible FIR lines at  $z \sim 6$  are hard to explain the luminosity ratio between the line and continuum. We thus conclude that these two lines are [C II] lines.
2. Our lens models, updated with the latest spectroscopic follow-up results with VLT/MUSE, suggest that these lines arise from a strongly magnified and multiply imaged ( $\mu \simeq 20 - 160$ ) Lyman-break galaxy (LBG) at  $z = 6.0719$  with a circularized effective radius of  $\sim 0.8 \text{ kpc}$  and an intrinsic luminosity in the rest-frame UV  $\sim 3$  times fainter ( $M_{\text{UV}} = -19.7_{-0.4}^{+0.5}$ ) than the characteristic luminosity at this epoch. A sub region of the LBG crosses the caustic line in the source plane and thus stretched into an arc over  $\sim 6''$  in the image plane, for which the [C II] line is also significantly detected. Our lens models also predict another two multiple images in this field. We identify the sources at the predicted positions and find that their optical–NIR colors agree with the other multiple images of the LBGs. One of them falls in the ALCS area coverage, where we detect a tentative [C II] line ( $3.0\sigma$ ) at the same frequency as the other multiple images.
  3. After the correction of the lensing magnification, the whole of the LBG and its sub region are characterized with  $L_{[\text{CII}]}$  of  $1.1_{-0.5}^{+0.7} \times 10^8$  and  $0.3_{-0.1}^{+0.1} \times 10^8 L_{\odot}$ , SFR of  $5.4_{-2.9}^{+4.5}$  and  $0.8_{-0.2}^{+0.4} M_{\odot} \text{ yr}^{-1}$ , and stellar mass ( $M_{\text{star}}$ ) of  $9.6_{-4.6}^{+6.0} \times 10^8$  and  $2.6_{-1.0}^{+0.2} \times 10^8 M_{\odot}$ , respectively. From the whole to sub regions of the LBG, the SFR and  $M_{\text{star}}$  values falls on the average relation among  $z \sim 6$  galaxies, indicating that the LBG is an abundant, representative galaxy at this epoch.
  4. The source plane reconstruction resolves the ISM down to  $\sim 100\text{--}300 \text{ pc}$ . The [C II] line from the whole region of the LBG is co-spatial with the rest-frame UV continuum, while the sub region of the LBG is placed  $\sim 1.6 \text{ kpc}$  away from the galactic center and bright rest-frame UV clumps. The two-peak morphology observed in the [C II] line and rest-frame FIR continuum in the arc show a  $\sim 1 \text{ kpc}$  offset from the luminosity-weighted center of the sub region of the LBG, which likely consists either of a clumpy structure or a smooth disk but stretched into the two-peak morphology due

to the perturbation by a foreground galaxy. In these two peaks, the [C II] line and the rest-frame FIR continuum exhibit the *flux ratio anomaly* differently, which suggests that the faint [C II]- and FIR-emitting regions are displaced near the caustic.

5. We find that our results in both whole and sub regions of the LBG fall on the SFR– $L_{[\text{CII}]}$  and surface density of SFR ( $\Sigma\text{SFR}$ )– $L_{[\text{CII}]}/\text{SFR}$  relations obtained in local star-forming galaxies. The sub region of the galaxy has a lower  $\Sigma\text{SFR}$  and a higher  $L_{[\text{CII}]}/\text{SFR}$  value. This is consistent with the absence of the bright rest-frame UV clumps around the sub region of the LBG that is placed  $\sim 1.6 \text{ kpc}$  away from the galactic center, where  $\Sigma\text{SFR}$  is expected to be low.
6. We find that the LBG is classified as a rotation-dominated system based on the full observed velocity gradient and the velocity dispersion of the LBG via the bright [C II] line emission. The 3D modeling with <sup>3D</sup>BAROLO and GALPAK3D provide consistent results for the rotation kinematics that explains the spatial and velocity offsets of the sub region of the LBG. We estimate the dynamical mass of  $M_{\text{dyn}} = (3 \pm 1) \times 10^9 M_{\odot}$  and obtain the gas fraction of  $\sim 50\text{--}80\%$ .
7. We derive a lower limit on the [C II] luminosity function at  $z = 6$ . We find that it is consistent with current semi-analytical model predictions. In conjunction with previous ALMA results, we also find that constraints on the [C II] luminosity function at  $z = 6$  so far obtained agree with the prediction from the SFR– $L_{[\text{CII}]}$  relation of local star-forming galaxies and the SFR function at  $z = 6$ .
8. With the blind aspect of the ALCS survey and the SFR– $L_{[\text{CII}]}$  relations from the sub to whole regions of the LBG, our results may imply that the local SFR– $L_{[\text{CII}]}$  relation is universal for a wide range of scales including the spatially resolved ISM, the whole region of the galaxy, and the cosmic scale even up to  $z = 6$ , which we derive in an unbiased manner.

We thank the anonymous referee for the careful review and valuable comments that improved the clarity of the paper. We thank Justin Spilker and Tanio Díaz-Santos for sharing their measurements. We also thank John R. Weaver and Yuchi Harikane for useful comments on the paper and Francesca Rizzo for helpful comments for the kinematic analysis. This paper makes use of the ALMA

data: ADS/JAO. ALMA #2018.1.00035.L. ALMA is a partnership of the ESO (representing its member states), NSF (USA) and NINS (Japan), together with NRC (Canada), MOST and ASIAA (Taiwan), and KASI (Republic of Korea), in cooperation with the Republic of Chile. The Joint ALMA Observatory is operated by the ESO, AUI/NRAO, and NAOJ. This work is based on observations and archival data made with the *Spitzer Space Telescope*, which is operated by the Jet Propulsion Laboratory, California Institute of Technology, under a contract with NASA along with archival data from the NASA/ESA *Hubble Space Telescope*. This research made also use of the NASA/IPAC Infrared Science Archive (IRSA), which is operated by the Jet Propulsion Laboratory, California Institute of Technology, under contract with the National Aeronautics and Space Administration. This work was supported in part by World Premier International Research Center Initiative (WPI Initiative), MEXT, Japan, and JSPS KAKENHI Grant Number JP18K03693. S.F. acknowledges support from the European Research Council (ERC) Consolidator Grant funding scheme (project ConTExt, grant No. 648179) and Independent Research Fund Denmark grant DFF-7014-00017. The Cosmic Dawn Center is funded by the Danish National Research Foundation under grant No. 140. NL acknowledges the Kavli Foundation. GBC and KIC acknowledge funding from the European Research Council through the Consolidator Grant ID 681627-BUILDUP. F.E.B acknowledges supports from ANID grants CATA-Basal AFB-170002, FONDECYT Regular 1190818, and 1200495, and Millennium Science Initiative ICN12.009. IRS acknowledges support from STFC (ST/T000244/1). KK acknowledges support from the Swedish Research Council and the Knut and Alice Wallenberg Foundation.

*Software:* CASA (v5.4.0; McMullin et al. 2007), GRIZLI (Brammer et al. 2008), DENDROGRAM (Goodman et al. 2009), GALFIT (Peng et al. 2010), EAZY (Brammer et al. 2008), SCARLET (Melchior et al. 2018), <sup>3D</sup>Barolo (Di Teodoro & Fraternali 2015), GALPAK3D (Bouché et al. 2015), GLAFIC (Oguri 2010), LENSTOOL (Jullo et al. 2007), LTM (Zitrin et al. 2015)

## APPENDIX

## A. MUSE SPECTROSCOPIC CATALOG

In Table 5, we summarize the spectroscopic sample from VLT/MUSE (ESO program ID 0100.A-0792, PI: A. Edge) which we use for constraining our lens mass models.

**Table 5.** MUSE Spectroscopic Catalog

RELICS ID	R.A.	Dec.	$z_{\text{spec}}$	flag
(1)	deg	deg	(4)	(5)
467	90.0386151	-20.1280873	0.0	4
474	90.0261297	-20.1283111	0.4366	2
490	90.0410860	-20.1282533	0.8943	3
508	90.0352780	-20.1293624	0.0	4
510	90.0366252	-20.1292593	0.4230	3
514	90.0389765	-20.1292234	0.4293	3
524	90.0333696	-20.1293114	0.5614	3
538	90.0258085	-20.1298490	1.0270	9
539	90.0260218	-20.1303021	0.4448	3
543	90.0333594	-20.1313998	0.4299	3
545	90.0346490	-20.1312617	0.4316	3
547	90.0322874	-20.1302526	0.4234	3
571	90.0288919	-20.1307349	0.8751	3
606	90.0317981	-20.1320082	0.2662	3
620	90.0264851	-20.1330304	0.3284	3
624	90.0292841	-20.1331843	0.4164	3
625	90.0286343	-20.1325697	0.3449	3
626	90.0288471	-20.1326848	0.3448	3
647	90.0377894	-20.1333237	0.4176	3
660	90.0400373	-20.1375945	0.3843	3
662	90.0412169	-20.1343049	0.384	3
684	90.0410355	-20.1343563	0.3838	3
685	90.0359084	-20.1336945	0.4190	2
687	90.0328670	-20.1339062	0.2298	3
697	90.0359808	-20.1344771	0.4215	3
699	90.0321831	-20.1357916	0.4245	2
705	90.0332455	-20.1367707	0.0	4
711	90.0349938	-20.1360342	0.4332	3
724	90.0265792	-20.1350258	0.7360	3
735	90.0274334	-20.1354704	0.4280	3
736	90.0257819	-20.1357459	0.4294	3
737	90.0267125	-20.1360004	0.4300	3
742	90.0340260	-20.1357916	0.4266	3
743	90.0376604	-20.1357714	0.4369	3
754	90.0337757	-20.1341905	0.4233	2
772	90.0278737	-20.1374801	0.4307	3

779	90.0326653	-20.1350609	0.4305	3
786	90.0429917	-20.1367709	5.4589	9
791	90.0281193	-20.1381123	0.5089	3
792	90.0335009	-20.1349955	0.4304	3
801	90.0394961	-20.1371561	4.5043	3
802	90.0348279	-20.1356744	0.4319	3
806	90.0364247	-20.1377419	0.4295	3
814	90.0414618	-20.1358813	0.0	4
823	90.0317133	-20.1382886	0.4276	3
836	90.0264868	-20.1381907	0.0	4
860	90.0365781	-20.1393201	0.4177	3
862	90.0279194	-20.1393703	0.4321	3
863	90.0278743	-20.1397608	0.4296	3
870	90.0430009	-20.1395918	0.4392	3
871	90.0425305	-20.1399135	0.3825	3
886	90.0419909	-20.1399491	0.4462	2
887	90.0340961	-20.1398346	0.4315	3
899	90.0295615	-20.1407949	0.4317	3
900	90.0296018	-20.1404579	0.4323	3
938	90.0430509	-20.1413250	0.4197	3
941	90.0343581	-20.1391201	0.4195	3
956	90.0355945	-20.1419747	0.4240	2
957	90.0387747	-20.1421929	0.4314	3
962	90.0306151	-20.1429810	0.0866	3
963	90.0303906	-20.1430867	0.0866	3
964	90.0304180	-20.1428506	0.0866	3
965	90.0304371	-20.1427616	0.0866	3
966	90.0299297	-20.1421244	0.0866	3
967	90.0300655	-20.1424500	0.0866	3
973	90.0349638	-20.1425005	0.4255	3
974	90.0350788	-20.1429515	0.4313	3
990	90.0258089	-20.1429104	0.5491	3
1000	90.0296362	-20.1430670	0.4305	3
1003	90.0384290	-20.1430473	0.5479	9
1024	90.0337998	-20.1436577	2.7722	3
1025	90.0340880	-20.1437083	2.7723	3
1027	90.0351249	-20.1438250	2.7723	9
1029	90.0356487	-20.1438539	2.7725	3
900001	90.0424970	-20.1364998	3.5238	3
900003	90.0283847	-20.1376962	5.4067	9

(1) ID from the RELICS public catalogue of `hlspec_relics_hst_wfc3ir_rxc0600-20_multi.v1_cat.txt`<sup>4</sup>. IDs start-

<sup>4</sup> <https://relics.stsci.edu/>

ing with 900 are MUSE detections with no counterpart in the mentioned catalogue. (2) Observed right ascension in degrees. (3) Observed declination in degrees. (4) MUSE spectroscopic redshift. (5) Redshift quality flag. 2: likely, 3: secure measurement, 9: single line measurement, and 4: field stars.

### B. TWO-PEAK MORPHOLOGY IN $z6.1/6.2$

To check the possibility that the two-peak morphology of the [C II] line in  $z6.1/6.2$  is caused by the noise fluctuation boosted by the underlying diffuse emission (e.g., Hodge et al. 2016), we perform a mock observation with the CASA task SIMOBSERVE towards  $z6.1/6.2$  in the same manner as Fujimoto et al. (2020a). Here we assume the single elliptical Gaussian for the [C II] line surface brightness distribution of  $z6.1/6.2$  based on the IMFIT results in the  $uv$ -tapered map (Section 3.1). We then obtain the visibility data set through SIMOBSERVE and produce the natural-weighted velocity-integrated map of the [C II] line. We repeat the mock observation to producing the map 1,000 times. Given that the spatial offset of  $\sim 2''.0$  and the significance levels of  $8.2\sigma$  and  $5.4\sigma$  between the two peaks in  $z6.1/6.2$ , we then search multiple positive peaks that are located with spatial offsets of less than  $2''.5$  and detected at  $\geq 5.4\sigma$  levels, utilizing SExtractor version 2.5.0 (Bertin & Arnouts 1996). We identify 7 out of 1,000 maps have the multiple peaks that meet the above criteria. These results indicate that the two-peak morphology of the [C II] line in  $z6.1/6.2$  might be caused by the noise fluctuation with a probability of  $\sim 0.7\%$ . Note that we find that all multiple peaks identified in the 7 maps show their flux ratios almost identical, which is different from the two peaks observed in  $z6.1/6.2$  (ratio  $\sim 8:5$ ). This indicates that the close separation as well as the flux ratio of the two peaks observed in  $z6.1/6.2$  is hardly explained by the noise fluctuation. In fact, we identify only 1 out of 1,000 maps that has a flux ratio of multiple peaks similar to the two peaks in  $z6.1/6.2$ , but with the spatial offset of  $4''.7$ . Therefore, we conclude that the possibility of the noise fluctuation is negligible in the two-peak [C II] line morphology of  $z6.1/6.2$ .

### C. OPTICAL-NIR PHOTOMETRY

We adopt separate strategies for extracting robust photometry for the four lensed images as described below to account for the crowded cluster field and varying degrees of extended source morphology. In general, we model the full IRAC mosaics using a strategy similar to that of Merlin et al. (2015), where we use image thumbnails of each source and neighbors taken from the high-resolution *HST*/WFC3 F160W image and knowledge of the WFC3 and IRAC point spread functions (PSFs) to model the low-resolution IRAC image.

#### C.1. Images $z6.3$ and $z6.5$

The sources of interest in these images are relatively bright and fairly well separated from their nearest bright (projected) neighbors (Figure 1). We measure aperture flux densities in each of the *HST* filters using fixed  $D = 0''.7$  apertures centered on the source of interest to define the colors. To determine the overall flux normalization, we model the source morphology of the lensed image and nearby neighbors using the non-parametric morphological fitting code SCARLET (Melchior et al. 2018). All of the WFC3/IR images (and their PSFs) are used to constrain the SCARLET morphological model. We scale all of the *HST* aperture measurements  $F_{ap,i}$  by the aperture correction  $F_{S,F160W}/F_{ap,F160W}$ , where  $F_{S,F160W}$  is the integral of the SCARLET model evaluated in the F160W filter and  $F_{S,F160W}$  is the aperture measurement in that filter. The photometric uncertainties are measured in the same apertures on the inverse variance image in each filter. For the IRAC flux densities of these images, we subtract all modeled sources other than the source of interest and perform aperture photometry on this cleaned image using  $D = 3''.0$  apertures, which we correct to the same “total” scale as for *HST* using aperture corrections of 1.6 and 1.7 for channels 1 and 2, respectively, that were derived from a separate bright, isolated source in the field.

#### C.2. Extended arc image $z6.1/6.2$

This image is a highly elongated arc extending over  $\approx 6$  arcsec coincident with a foreground compact source in the center (Figure 1). Here, we model both overlapping sources in the F160W image as parametric Sersic profiles using the GALFIT software (Peng et al. 2010). For the photometry of the lensed arc and foreground image in the WFC3/IR filters, we fit for the relative normalizations of the two Sersic components convolved with the appropriate PSFs. For IRAC, we convolve the model Sersic profiles with the IRAC PSF and fit for the normalization of the source of interest and all neighboring sources in the least-squares optimization. As for *HST*, the normalization of the scaled morphological components is adopted as the photometric measurement without additional aperture corrections. For the optical images where the arc is not readily visible, we measure an aperture flux density and its associated uncertainty within a large rectangle aperture approximately  $1''.2 \times 3''.0$ .

Note that the de-blended color of the foreground object is similar to the color of cluster members, and the best-fit SED shows the photometric redshift at  $0.57^{+0.14}_{-0.17}$  which is close to the cluster redshift at  $z = 0.43$  (see also Laporte et al. submitted). Although this suggests the

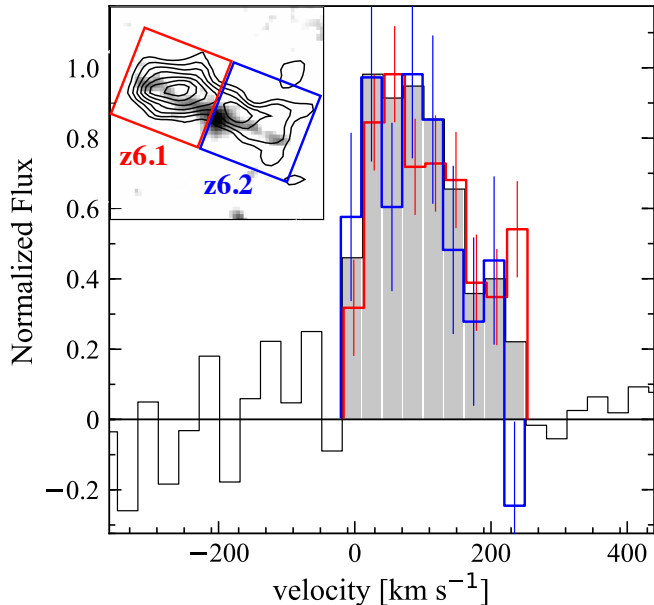


**Figure 10.** Zoom-in [C II] line spectra of  $z6.1$  and  $z6.2$  as a function of velocity with respect to the frequency peak of  $z6.3$ . The inset panel shows the same image cutout as the middle panel of Figure 1 for  $z6.1/6.2$ . The red and blue squares denote apertures that are used to produce the [C II] spectra for  $z6.1$  and  $z6.2$ , respectively. The black line and the grey shade indicate the integrated [C II] line spectrum of  $z6.1/6.2$  and the [C II]-detected channels, respectively. The red and blue lines present the [C II] spectra for  $z6.1$  and  $z6.2$ , respectively, that are normalized to the peak of the integrated one.

foreground to be one of the cluster members, we do not include it in our fiducial mass model due to potential systematics in the de-blending process. The detail contribution of the foreground object to morphology and magnification factors of  $z6.1/6.2$  (Section 4.1) must be investigated after we obtain the spectroscopic redshift of the foreground object.

### C.3. Faint image $z6.4$

The final faint image of  $z6.4$  is close to the cluster core and the BCG. Although it is not deblended as a separate source in our original photometric catalog (and associated IRAC model), a source is readily apparent in the F160W image (Figure 1). We estimate photometry of this image by placing fixed  $D = 0''.7$  and  $D = 3''.0$

apertures centered on the F160W position in the *HST* and IRAC filter mosaics, respectively, and scale these measurements by aperture corrections derived for point sources.

### D. [C II] SPECTRA OF $z6.1$ AND $z6.2$

As a sanity check of our interpretation that one of the [C II] line emitters consists of a pair of multiple images of  $z6.1$  and  $z6.2$ , we compare [C II] spectra between  $z6.1$  and  $z6.2$ . In Figure 10, we show the [C II] spectra of  $z6.1$  (red line) and  $z6.2$  (blue line) that are normalized to the peak of  $z6.1/6.2$  (black line). We find that  $z6.1$  and  $z6.2$  have [C II] line profiles consistent with each other within the errors, which agrees with our interpretation of  $z6.1$  and  $z6.2$  being a pair of multiple images.

### E. [C II] ROTATION MODELING

In Section 4.2, we find that  $z6.3$  is likely a rotation-dominated system. In Table 6, we summarize the 3D modeling results for the [C II] line around  $z6.3$  with <sup>3D</sup>BAROLO (Di Teodoro & Fraternali 2015) and GALPAK3D (Bouché et al. 2015). For <sup>3D</sup>BAROLO, because the ALMA beam has a half-width-at-half-maximum (HWHM) of  $\sim 0''.45$  at the [C II] line frequency along the orientation of the velocity gradient, we adopt three ( $\sim 1.4/0.45$ ) annuli with the width of  $0''.45$  for the tilted ring fitting algorithm. We use the THRESHOLD mask with the  $2\sigma$  limit for the data cube, and the spatial center, systemic velocity, rotation velocity ( $v_{\text{rot}}$ ), velocity dispersion ( $\sigma_{\text{vel}}$ ), position angle (PA), and inclination (incl.) are used as free parameters in the fitting. The errors are estimated based on the minimization algorithm in a Monte Carlo approach. For GALPAK3D, we adopt the exponential-disk for the flux profile, the Gaussian for the thickness profile, and the tanh formalization of  $V_{\text{max}} \times \tanh(r/r_V)$  for the rotation curve, where  $V_{\text{max}}$  and  $r_V$  are the maximum velocity and the turnover radius, respectively. In place of the mask, we use a cutout data cube by  $3''.8 \times 3''.8$  and  $[-120: +120]$   $\text{km s}^{-1}$  for the fitting. We set the maximum iteration number of 20,000. The spatial center, systemic velocity, flux,  $r_e$ , PA, incl.,  $r_V$ ,  $V_{\text{max}}$ , and  $\sigma_{\text{vel}}$  are used as free parameters. The errors are evaluated based on a Markov chain Monte Carlo approach.

## REFERENCES

Aravena, M., Decarli, R., Walter, F., et al. 2016, ApJ, 833,

Bacon, R., Piqueras, L., Conseil, S., Richard, J., & Shepherd, M. 2016, MPDAF: MUSE Python Data Analysis Framework, ascl:1611.003

**Table 6.** 3D Modeling Results

	${}^{3D}$ BAROLO			GALPAK3D
	Ring1	Ring2	Ring3	Exponential disk
radius <sup>a</sup> ["]	0–0.45	0.45–0.9	0.9–1.35	$0.55 \pm 0.02$
$v_{\text{LOS}}^b$ [km s <sup>-1</sup> ]	$22_{-4}^{+5}$	$76_{-22}^{+22}$	$62_{-3}^{+4}$	$62 \pm 4$
$\sigma_{\text{vel}}$ [km s <sup>-1</sup> ]	$46_{-8}^{+9}$	$54_{-11}^{+11}$	$59_{-7}^{+7}$	$55 \pm 3$
incl. [deg]	56	57	59	$57 \pm 3$
PA <sup>c</sup> [°]	36	32	27	$21 \pm 3$

*a* Inner and outer radii of the tilted rings for  ${}^{3D}$ BAROLO and effective radius for GALPAK3D. The turnover radius is estimated to be  $0''.62 \pm 0''.11$  in the tanh formalization for the rotation curve in GALPAK3D.

*b* Line-of-sight projected rotation velocity. We present  $V_{\text{max}}$  for GALPAK3D.

*c* We follow the definition of PA as the orientation from the y-axis in anti-clockwise, which is different from that of the original output of  ${}^{3D}$ BAROLO.

Bakx, T. J. L. C., Tamura, Y., Hashimoto, T., et al. 2020, MNRAS, 493, 4294

Bell, E. F., Papovich, C., Wolf, C., et al. 2005, ApJ, 625, 23

Bertin, E., & Arnouts, S. 1996, A&A, 117, 393

B  thermin, M., Fudamoto, Y., Ginolfi, M., et al. 2020, A&A, 643, A2

Bouch  , N., Carfantan, H., Schroetter, I., Michel-Dansac, L., & Contini, T. 2015, AJ, 150, 92

Bouwens, R. J., van Dokkum, P. G., Illingworth, G. D., et al. 2017, ArXiv e-prints, arXiv:1711.02090

Bowler, R. A. A., Bourne, N., Dunlop, J. S., McLure, R. J., & McLeod, D. J. 2018, MNRAS, 481, 1631

Brammer, G. B., van Dokkum, P. G., & Coppi, P. 2008, ApJ, 686, 1503

Brauher, J. R., Dale, D. A., & Helou, G. 2008, The Astrophysical Journal Supplement Series, 178, 280

Calura, F., Vanzella, E., Carniani, S., et al. 2021, MNRAS, 500, 3083

Calzetti, D., Armus, L., Bohlin, R. C., et al. 2000, ApJ, 533, 682

Caminha, G. B., Grillo, C., Rosati, P., et al. 2017, A&A, 607, A93

Caminha, G. B., Rosati, P., Grillo, C., et al. 2019, A&A, 632, A36

Carniani, S., Maiolino, R., Amorin, R., et al. 2018, MNRAS, 478, 1170

Carniani, S., Gallerani, S., Vallini, L., et al. 2019, MNRAS, 489, 3939

Carniani, S., Ferrara, A., Maiolino, R., et al. 2020, arXiv e-prints, arXiv:2006.09402

Chabrier, G. 2003, PASP, 115, 763

Chambers, K. C., Magnier, E. A., Metcalfe, N., et al. 2016, arXiv e-prints, arXiv:1612.05560

Chapin, E. L., Pope, A., Scott, D., et al. 2009, MNRAS, 398, 1793

Coe, D., Salmon, B., Brada  , M., et al. 2019, ApJ, 884, 85

Conroy, C., & Gunn, J. E. 2010, ApJ, 712, 833

Conroy, C., Gunn, J. E., & White, M. 2009, ApJ, 699, 486

Cooke, E. A., Smail, I., Swinbank, A. M., et al. 2018, ApJ, 861, 100

De Barros, S., Pentericci, L., Vanzella, E., et al. 2017, A&A, 608, A123

De Looze, I., Cormier, D., Leboutteiller, V., et al. 2014, A&A, 568, A62

Decarli, R., Aravena, M., Boogaard, L., et al. 2020, arXiv e-prints, arXiv:2009.10744

Dessauges-Zavadsky, M., Zamojski, M., Rujopakarn, W., et al. 2017, A&A, 605, A81

Dessauges-Zavadsky, M., Richard, J., Combes, F., et al. 2019, Nature Astronomy, 3, 1115

Dessauges-Zavadsky, M., Ginolfi, M., Pozzi, F., et al. 2020, arXiv e-prints, arXiv:2004.10771

Di Teodoro, E. M., & Fraternali, F. 2015, MNRAS, 451, 3021

D  az-Santos, T., Armus, L., Charmandaris, V., et al. 2013, ApJ, 774, 68

Dye, S., Furlanetto, C., Swinbank, A. M., et al. 2015, MNRAS, 452, 2258

Ebeling, H., Edge, A. C., & Henry, J. P. 2001, ApJ, 553, 668

Faisst, A. L., Fudamoto, Y., Oesch, P. A., et al. 2020, MNRAS, arXiv:2005.07716

Ferrara, A., Vallini, L., Pallottini, A., et al. 2019, MNRAS, 489, 1

Finkelstein, S. L., Papovich, C., Dickinson, M., et al. 2013, Nature, 502, 524

Flewelling, H. A., Magnier, E. A., Chambers, K. C., et al. 2016, arXiv e-prints, arXiv:1612.05243

F  rster Schreiber, N. M., Genzel, R., Bouch  , N., et al. 2009, ApJ, 706, 1364

Fujimoto, S., Oguri, M., Nagao, T., Izumi, T., & Ouchi, M. 2020a, ApJ, 891, 64

Fujimoto, S., Ouchi, M., Shibuya, T., & Nagai, H. 2017, ApJ, 850, 1

Fujimoto, S., Ouchi, M., Ferrara, A., et al. 2019, ApJ, 887, 107

Fujimoto, S., Silverman, J. D., Bethermin, M., et al. 2020b, arXiv e-prints, arXiv:2003.00013

Gaia Collaboration, Brown, A. G. A., Vallenari, A., et al. 2018, A&A, 616, A1

- Gallerani, S., Pallottini, A., Feruglio, C., et al. 2018, *MNRAS*, 473, 1909
- Gehrels, N. 1986, *ApJ*, 303, 336
- Ginolfi, M., Jones, G. C., Béthermin, M., et al. 2020, *A&A*, 633, A90
- González-López, J., Bauer, F. E., Aravena, M., et al. 2017, *A&A*, 608, A138
- Goodman, A. A., Rosolowsky, E. W., Borkin, M. A., et al. 2009, *Nature*, 457, 63
- Gullberg, B., Swinbank, A. M., Smail, I., et al. 2018, *ApJ*, 859, 12
- Harikane, Y., Ouchi, M., Shibuya, T., et al. 2018, *ApJ*, 859, 84
- Harikane, Y., Ouchi, M., Inoue, A. K., et al. 2020, *ApJ*, 896, 93
- Hashimoto, T., Laporte, N., Mawatari, K., et al. 2018, *Nature*, 557, 392
- Hashimoto, T., Inoue, A. K., Mawatari, K., et al. 2019, *PASJ*, 71, 71
- Hatsukade, B., Tamura, Y., Iono, D., et al. 2015, *PASJ*, 67, 93
- Hayatsu, N. H., Matsuda, Y., Umehata, H., et al. 2017, *PASJ*, 69, 45
- Hayatsu, N. H., Ivison, R. J., Andreani, P., et al. 2019, *Research Notes of the American Astronomical Society*, 3, 97
- Herrera-Camus, R., Bolatto, A. D., Wolfire, M. G., et al. 2015, *ApJ*, 800, 1
- Higuchi, R., Ouchi, M., Ono, Y., et al. 2019, *ApJ*, 879, 28
- Hodge, J. A., Swinbank, A. M., Simpson, J. M., et al. 2016, *ApJ*, 833, 103
- Holwerda, B. W., Bouwens, R., Oesch, P., et al. 2015, *ApJ*, 808, 6
- Inoue, A. K., Tamura, Y., Matsuo, H., et al. 2016, *Science*, 352, 1559
- Iye, M., Ota, K., Kashikawa, N., et al. 2006, *Nature*, 443, 186
- Iyer, K., Gawiser, E., Davé, R., et al. 2018, *ApJ*, 866, 120
- Jones, G. C., Carilli, C. L., Shao, Y., et al. 2017, *ApJ*, 850, 180
- Jullo, E., Kneib, J. P., Limousin, M., et al. 2007, *New Journal of Physics*, 9, 447
- Kawamata, R., Ishigaki, M., Shimasaku, K., et al. 2018, *ApJ*, 855, 4
- Kawamata, R., Oguri, M., Ishigaki, M., Shimasaku, K., & Ouchi, M. 2016, *ApJ*, 819, 114
- Knudsen, K. K., Richard, J., Kneib, J.-P., et al. 2016, *MNRAS*, 462, L6
- Kohandel, M., Pallottini, A., Ferrara, A., et al. 2019, *MNRAS*, 487, 3007
- Kriek, M., & Conroy, C. 2013, *ApJ*, 775, L16
- Kusakabe, H., Blaizot, J., Garel, T., et al. 2020, arXiv e-prints, arXiv:2003.12083
- Lagache, G., Cousin, M., & Chatzikos, M. 2018, *A&A*, 609, A130
- Laporte, N., Katz, H., Ellis, R. S., et al. 2019, *MNRAS*, 487, L81
- Le Fèvre, O., Béthermin, M., Faisst, A., et al. 2020, *A&A*, 643, A1
- Loiacono, F., Decarli, R., Gruppioni, C., et al. 2020, arXiv e-prints, arXiv:2006.04837
- Lotz, J. M., Koekemoer, A., Coe, D., et al. 2017, *ApJ*, 837, 97
- Magdis, G. E., Rigopoulou, D., Hopwood, R., et al. 2014, *The Astrophysical Journal*, 796, 63
- Maiolino, R., & Mannucci, F. 2019, *A&A Rev.*, 27, 3
- Maiolino, R., Carniani, S., Fontana, A., et al. 2015, *MNRAS*, 452, 54
- Malhotra, S., Kaufman, M. J., Hollenbach, D., et al. 2001, *ApJ*, 561, 766
- Mao, S., & Schneider, P. 1998, *MNRAS*, 295, 587
- Matsuda, Y., Nagao, T., Iono, D., et al. 2015, *MNRAS*, 451, 1141
- Matthee, J., Sobral, D., Gronke, M., et al. 2020, *MNRAS*, 492, 1778
- Matthee, J., Sobral, D., Boone, F., et al. 2017, *ApJ*, 851, 145
- Matthee, J., Sobral, D., Boogaard, L. A., et al. 2019, *ApJ*, 881, 124
- McMullin, J. P., Waters, B., Schiebel, D., Young, W., & Golap, K. 2007, in *Astronomical Society of the Pacific Conference Series*, Vol. 376, *Astronomical Data Analysis Software and Systems XVI*, ed. R. A. Shaw, F. Hill, & D. J. Bell, 127
- Melchior, P., Moolekamp, F., Jerdee, M., et al. 2018, *Astronomy and Computing*, 24, 129
- Merlin, E., Fontana, A., Ferguson, H. C., et al. 2015, *A&A*, 582, A15
- Murphy, E. J., Condon, J. J., Schinnerer, E., et al. 2011, *ApJ*, 737, 67
- Navarro, J. F., Frenk, C. S., & White, S. D. M. 1997, *ApJ*, 490, 493
- Novak, M., Bañados, E., Decarli, R., et al. 2019, *ApJ*, 881, 63
- Novak, M., Venemans, B. P., Walter, F., et al. 2020, *ApJ*, 904, 131
- Oesch, P. A., van Dokkum, P. G., Illingworth, G. D., et al. 2015, *ApJ*, 804, L30
- Oesch, P. A., Brammer, G., van Dokkum, P. G., et al. 2016, *ApJ*, 819, 129

- Oguri, M. 2010, PASJ, 62, 1017
- Oke, J. B., & Gunn, J. E. 1983, ApJ, 266, 713
- Ono, Y., Ouchi, M., Mobasher, B., et al. 2012, ApJ, 744, 83
- Ono, Y., Ouchi, M., Harikane, Y., et al. 2018, PASJ, 70, S10
- Pavesi, R., Riechers, D. A., Capak, P. L., et al. 2016, ApJ, 832, 151
- Peng, C. Y., Ho, L. C., Impey, C. D., & Rix, H.-W. 2010, AJ, 139, 2097
- Pentericci, L., Fontana, A., Vanzella, E., et al. 2011, ApJ, 743, 132
- Pentericci, L., Vanzella, E., Fontana, A., et al. 2014, ApJ, 793, 113
- Pentericci, L., Carniani, S., Castellano, M., et al. 2016, ApJ, 829, L11
- Pentericci, L., Vanzella, E., Castellano, M., et al. 2018, A&A, 619, A147
- Piqueras, L., Conseil, S., Shepherd, M., et al. 2017, arXiv e-prints, arXiv:1710.03554
- Planck Collaboration, Abergel, A., Ade, P. A. R., et al. 2011, A&A, 536, A21
- Popping, G., van Kampen, E., Decarli, R., et al. 2016, MNRAS, 461, 93
- Postman, M., Coe, D., Benítez, N., et al. 2012, ApJS, 199, 25
- Rizzo, F., Vegetti, S., Powell, D., et al. 2020, Nature, 584, 201
- Roberts-Borsani, G. W., Bouwens, R. J., Oesch, P. A., et al. 2016, ApJ, 823, 143
- Romano, M., Cassata, P., Morselli, L., et al. 2020, MNRAS, 496, 875
- Rybak, M., Hodge, J. A., Vegetti, S., et al. 2020, MNRAS, 494, 5542
- Rybak, M., McKean, J. P., Vegetti, S., Andreani, P., & White, S. D. M. 2015, MNRAS, 451, L40
- Schaerer, D., Ginolfi, M., Béthermin, M., et al. 2020, arXiv e-prints, arXiv:2002.00979
- Shibuya, T., Kashikawa, N., Ota, K., et al. 2012, ApJ, 752, 114
- Shibuya, T., Ouchi, M., & Harikane, Y. 2015, ApJS, 219, 15
- Shibuya, T., Ouchi, M., Harikane, Y., et al. 2018, PASJ, 70, S15
- Smit, R., Bouwens, R. J., Labbé, I., et al. 2016, ApJ, 833, 254
- Smit, R., Bouwens, R. J., Carniani, S., et al. 2018, Nature, 553, 178
- Soto, K. T., Lilly, S. J., Bacon, R., Richard, J., & Conseil, S. 2016, MNRAS, 458, 3210
- Spilker, J. S., Marrone, D. P., Aravena, M., et al. 2016, ApJ, 826, 112
- Spilker, J. S., Aravena, M., Béthermin, M., et al. 2018, Science, 361, 1016
- Stark, D. P., Ellis, R. S., & Ouchi, M. 2011, ApJ, 728, L2
- Stark, D. P., Ellis, R. S., Charlot, S., et al. 2017, MNRAS, 464, 469
- Strait, V., Bradač, M., Coe, D., et al. 2020, ApJ, 888, 124
- Swinbank, A. M., Smail, I., Longmore, S., et al. 2010, Nature, 464, 733
- Swinbank, A. M., Karim, A., Smail, I., et al. 2012, MNRAS, 427, 1066
- Swinbank, A. M., Vernet, J. D. R., Smail, I., et al. 2015, MNRAS, 449, 1298
- Tamura, Y., Oguri, M., Iono, D., et al. 2015, PASJ, 67, 72
- Tamura, Y., Mawatari, K., Hashimoto, T., et al. 2019, ApJ, 874, 27
- Tilvi, V., Papovich, C., Finkelstein, S. L., et al. 2014, ApJ, 794, 5
- Treu, T., Schmidt, K. B., Trenti, M., Bradley, L. D., & Stiavelli, M. 2013, ApJ, 775, L29
- Vallini, L., Gallerani, S., Ferrara, A., Pallottini, A., & Yue, B. 2015, ApJ, 813, 36
- Vanzella, E., Pentericci, L., Fontana, A., et al. 2011, ApJ, 730, L35
- Vanzella, E., Meneghetti, M., Caminha, G. B., et al. 2020, MNRAS, 494, L81
- Weilbacher, P. M., Streicher, O., Urrutia, T., et al. 2014, in Astronomical Society of the Pacific Conference Series, Vol. 485, Astronomical Data Analysis Software and Systems XXIII, ed. N. Manset & P. Forshay, 451
- Williams, J. P., de Geus, E. J., & Blitz, L. 1994, ApJ, 428, 693
- Yamaguchi, Y., Kohno, K., Tamura, Y., et al. 2017, ApJ, 845, 108
- Yan, L., Sajina, A., Loiacono, F., et al. 2020, arXiv e-prints, arXiv:2006.04835
- Zanella, A., Daddi, E., Magdis, G., et al. 2018, Monthly Notices of the Royal Astronomical Society, 481, 1976
- Zitrin, A., Fabris, A., Merten, J., et al. 2015, ApJ, 801, 44